Front matter

Title

A balance between actin and Eps8/IRSp53 utilization in branched versus linear actin networks determines tunneling nanotube formation

Authors

J. Michael Henderson[1,2,†,✉], Nina Ljubojevic[1,3,†], Thibault Chaze[4], Daryl Castaneda[1,5], Aude Battistella[2], Quentin Giai Gianetto[4,6], Mariette Matondo[4], Stéphanie Descroix[2,7], Patricia Bassereau[2,✉], and Chiara Zurzolo[1,✉].

Affiliations

1. Membrane Traffic and Pathogenesis Unit, Department of Cell Biology and Infection, CNRS UMR 3691, Université de Paris, Institut Pasteur, 75015 Paris, France.
2. Institut Curie, Université PSL, Sorbonne Université, CNRS UMR168, Laboratoire Physico-Chimie Curie, 75005 Paris, France.
3. Sorbonne Université, Doctoral School ED394, 75006 Paris, France.
4. Proteomics Platform, Mass Spectrometry for Biology Unit, CNRS USR 2000, Institut Pasteur, 75015 Paris, France.
5. Keele University, Keele, Staffordshire, ST5 5BG United Kingdom.
6. Bioinformatics and Biostatistics Hub, Computational Biology Department, CNRS USR 3756, Institut Pasteur, 75015 Paris, France.
7. Institut Pierre-Gilles de Gennes, 75005 Paris, France.

† These authors contributed equally to this work.

✉ Corresponding authors. Emails:

michael.henderson@pasteur.fr

patricia.bassereau@curie.fr

chiara.zurzolo@pasteur.fr

Abstract (218 words)

Tunneling nanotubes (TNTs) connect distant cells and mediate cargo transfer for intercellular communication in physiological and pathological contexts. How cells generate these actin-mediated protrusions to span lengths beyond those attainable by canonical filopodia remains unknown. Through a combination of micropatterning, microscopy and optical tweezer-based approaches, we demonstrate that TNTs forming through the outward extension of actin (not through cellular dislodgement) achieve distances greater than the mean length of filopodia, and that branched Arp2/3-dependent pathways attenuate the extent to which actin polymerizes in nanotubes, limiting TNT occurrence. Proteomic analysis using Epidermal growth factor receptor kinase substrate 8 (Eps8) as a positive effector of TNTs showed that upon Arp2/3 inhibition, proteins enhancing filament turnover and depolymerization were reduced and Eps8 instead exhibited heightened interactions with the inverted Bin/Amphiphysin/Rvs (I-BAR) domain protein IRSp53 that provides a direct connection with linear actin polymerases. Our data reveals how common protrusion players (Eps8 and IRSp53) form TNTs, and that when competing pathways overutilizing such proteins and monomeric actin in Arp2/3 networks are inhibited, processes promoting linear actin growth dominate to favour TNT formation. Thus, this work reinforces a general principle for actin network control for cellular protrusions where simple shifts in the balance between processes that inhibit actin growth versus those that promote growth dictate protrusion formation and the ultimate length scales protrusions achieve.

Main (4006 words)

Intercellular communication is vital for organisms, mediating across different length scales events like differentiation, tissue development/homeostasis, and wound healing. One mechanism relies on filamentous actin (F-actin)-based protrusions (*1*). Projecting a few microns from the cell, filopodia dynamically probe the environment, establishing focal adhesions or cell-cell connections for collective migration (*2*), tissue closure (*3*), and neurogenesis (*4*). Contrastingly, tunneling nanotubes (TNTs) are able to reach significantly longer distances (tens of microns) for direct communication between distant cells (*5*) and appear structurally different from filopodia (*6*).

First documented in 2004 (*7*, *8*), TNTs are non-surface adherent, membranous extensions supported by F-actin that cytoplasmically connect cells allowing the transfer of cargo ranging from Ca^{2+} ions (*9*), RNAs (*10*) and plasma membrane (PM) proteins (e.g., H-Ras, Fas/CD95) (*11*, *12*), to lysosomes (*13*) and mitochondria (*6*, *14*, *15*). This material transport ability has transformed the way we think about cell identity and the establishment of cellular networks (*16*, *17*). For example, *in vivo* evidence has supported a physiological role for TNT-like structures in vascular coupling within the retina (*18*) and in facilitating cytoplasmic and membrane-bound material transfer between photoreceptors (*19*, *20*), implicating nanotube-mediated maintenance in proper tissue function within the nervous system. Beyond their physiological involvement in signal transduction, apoptosis and immune responses (*12*, *21*), TNTs can contribute to cancer progression (*15*), HIV-1 and SARS-CoV-2 transmission (*22*, *23*), and the propagation of misfolded proteins (e.g., α-synuclein, Tau, huntingtin) involved in neurodegenerative diseases (*13*, *24–26*).

For protrusions to form, F-actin remodelling processes (initiation, polymerization and bundle stabilization) need to be spatiotemporally controlled at the PM in order to work against membrane tension resistance to form a tube (*27*). Proteins like IRSp53 (insulin receptor tyrosine kinase

substrate protein of 53 kDa) of the Bin/Amphiphysin/Rvs (BAR) family orchestrate membrane shape changes and actin assembly in filopodia, microvilli, and dendritic spine formation (*28–30*). Through its crescent-shaped inverse BAR domain IRSp53 is able to induce, sense and stabilize negative curvatures found in cellular protrusions (*31*, *32*). Its CRIB (Cdc42/Rac interactive binding) domain permits regulatory control by Rho GTPases (*28*, *33*), while its SH3 (Src homology 3) domain mediates interactions with actin polymerases like VASP (vasodilator-stimulated phosphoprotein) (*28*, *34*) and the formin mDia1 (*35*), and nucleating promoting factors of the actin-related protein 2/3 (Arp2/3) complex like N-WASP (*36*) and WAVE2 (*35*, *37*). Thus, IRSp53 self-assembly at the PM is sufficient to generate forces for protrusion growth by recruiting polymerases and locally polymerizing F-actin at IRSp53 clusters (*28*, *38*).

A key partner of I-BAR proteins in filopodia and microvilli formation is Eps8 (epidermal growth factor receptor kinase substrate 8) (*33*, *39*, *40*). Eps8 was identified in a complex with Abi-1 (Abelson interactor 1) and Sos-1 (Son of sevenless homolog 1) that activates Rac (*41*, *42*) for branched actin formation by Arp2/3 (*43*). Eps8 displays actin regulatory behaviour that depends on its binding partners: interaction with IRSp53 enhances Eps8's F-actin bundling activity, while binding with Abi-1 prompts its capping activity (*33*, *34*, *44*, *45*). We recently demonstrated that Eps8's actin bundling activity promotes the formation of functional TNTs in neuronal cells (*46*), suggesting a switch in common actin-regulating components in generating shorter canonical filopodia versus longer TNTs. The mechanism(s) by which the cell uses a common pool of actin-interfacing proteins to establish length scales characteristic of TNTs is unclear.

To address this issue, we used micropatterning to control the distances over which actin-dependent processes, and not mechanisms based on cell dislodgement, lead to TNT formation at lengths beyond those of canonical filopodia. We found that Arp2/3-dependent pathways deter TNTs and that upon Arp2/3 inhibition, F-actin polymerizes over longer distances in nanotubes. Arp2/3 inhibition further promoted a specific interaction between Eps8 and IRSp53, and not with other I-BAR proteins, and their co-expression facilitated functional TNT formation. Proteomic analysis revealed that Eps8's interactions with branched actin networks and proteins influencing filament turnover and depolymerization are reduced upon Arp2/3 inhibition, while IRSp53's interactome remained unchanged and provided connections to needed polymerases. Our data show that protrusion length results from a competing balance between the utilization of monomeric actin and the availability of actin regulatory proteins in order to build distinct F-actin networks in a common cytoplasm.

Results

TNTs connect micropatterned cells at greater distances compared to filopodia

To assess TNT formation as a function of intercellular distances, we fabricated hexagonal arrays of fibronectin (FN) micropatterns to tune the separation distance *D* (Fig. 1a, b and Supplementary Fig. 1a) to be beyond the reach of filopodia which typically ranges 1–2 µm and rarely exceeds 10 µm (*1*, *27*). CAD cell adherence was optimized on appropriately sized patterns to prevent unwanted cell infiltration into the surrounding PEG region (Supplementary Fig. 1b–e and Supplementary Video 1), ensuring that the connections we observe come from actin-driven mechanisms, and not from cells that migrate apart forming TNTs through cell dislodgement (*5*, *47*). Overnight cell tracking (18 hr) confirmed that CAD cells remained resident to their initial

micropatterns (Supplementary Fig. 1f, g, Example 1 and Supplementary Video 2), even during mitosis (Supplementary Fig. 1g, Example 3 and Supplementary Video 3), and cells rarely exhibited events of inter-micropattern translocation (Supplementary Fig. 1g, Example 2 and Supplementary Video 4).

We identified thin, substrate-detached TNT-like protrusions positive for F-actin connecting cells on neighbouring patterns at 15 to 30 µm (Fig. 1c, d), and containing DiD-labelled vesicles (Supplementary Fig. 2a). Using a donor-acceptor co-culture (Supplementary Fig. 2b) we found DiD vesicles both in the histone 2B (H2B)-positive acceptor cells (Supplementary Fig. 2c, Example 1) and in the connecting TNTs (Supplementary Fig. 2c, Example 2) supporting cargo transport. After increasing *D* to 40 µm, we observed fewer TNTs (Fig. 1e). *D*15 and *D*20 patterns showed the highest TNT frequency, while approaching *D*40, there was a significant decrease (Fig. 1f), indicating a distance dependency. On the other hand, filopodia lengths showed that a majority of filopodia (90% of the population) were far shorter and did not exceed 6 µm with an average length of 2.7 µm (Fig. 1g). These data show that TNTs are able to reach considerably longer lengths than average filopodia, yet there seems to be an upper limit to F-actin based elongation.

Inhibition of branched actin networks favours TNTs

Actin assembly can be organized into distinct architectures such as Arp2/3-dependent branched filaments in lamellipodia, or bundles of un-branched linear filaments. Phenotypic characterization of TNT-connected cells on *D*15 micropatterns revealed that cells displaying only lamellipodia accounted for 4.1% of TNTs examined (Fig. 2a, b). In contrast, in 71.1% of cases both cells involved in the connection had no lamellipodia (Fig 2a, b) while 24.7% of these TNT-connected cells had a mix of cellular phenotypes (Fig. 2a, b). Further analysis revealed that TNTs rarely emerge directly from lamellipodia (< 2% of cases) and instead originate either further up on the cell body or from protrusion-rich zones (Supplementary Fig. 3). Together, this suggests an anti-correlation between regions with high Arp2/3 activity and a cell's ability to form TNTs.

We next assessed if the inhibition of actin incorporation in Arp2/3-dependent networks favours the formation of TNTs. Upon Arp2/3 inhibition with CK-666 (*6*, *48*), we observed a significant increase in the percent of TNT-connected cells on *D*15, *D*20 and *D*30 micropatterns (Fig. 2c). In contrast, CK-666 had no impact on the number of TNT-connected cells on *D*40 patterns (Fig. 2c) again suggesting there is an upper limit to the length a TNT can obtain through the polymerization of actin (Fig. 1f and Fig. 2c). We hypothesized that a competition between different actin networks has a direct effect on the likelihood for a TNT to form over a given distance. Thus we directly shifted the actin balance in favour of linear F-actin by using the formin-specific agonist drug IMM-01 (*49*) and assessed the effect on TNTs. With IMM-01 treatment, we observed an increased number of TNT-connected cells (Supplementary Fig. 4a, b) and of vesicles transferred from donor to acceptor cells (Supplementary Fig. 4c), indicating that the promotion of linear actin networks directly favours functional TNT formation. Together this data suggests that TNT formation is based on the polymerization of long, linear filaments and becomes enhanced when branched actin formation is inhibited.

F-actin polymerization occurs over longer distances when Arp2/3 is inhibited

To gain a greater insight into how TNTs can reach longer distances, we utilized an optical tweezer (OT) setup to pull nanotubes of comparable lengths to the TNTs observed on the micropatterns to monitor by confocal microscopy F-actin polymerization within the nanotube in control and CK-666-treated conditions (Fig. 3a) (*38*, *50–52*). In the mock condition, cells displayed little to no F-actin within the nanotubes (Fig. 3b, c and Supplementary Video 5). In contrast, CK-666-treated cells showed a robust development of F-actin (Fig. 3d, e and Supplementary Video 6). Profiles of the F-actin fluorescence showed a rapid decay of the signal in mock-treated cells where intensity values were indistinguishable from background levels beyond 5 µm; however, CK-666-treated cells exhibited a shallower decay and intensities remained higher throughout the entire nanotube (Fig. 3c, e).

Exponential fitting of the actin profiles (Fig. 3f) and force measurements (Fig. 3g, h) confirmed CK-666-treated cells had F-actin reaching significantly longer distances within the nanotube compared to mock conditions. For example, force profiles remained static over time in control conditions for actin-devoid nanotubes (Fig. 3g), whereas large bead displacements (i.e., a rise in the force, ΔF) were observed in the CK-666 condition (Fig. 3h), indicating that F-actin development had reached the end of the tube, imparting large traction forces (Fig. 3i). This characteristic actin-dependent behaviour has been described previously by us and others (*38*, *50*, *51*, *53*). These data indicate that an inhibition of Arp2/3 activity directly correlates with the polymerization of longer actin filaments.

An Eps8-IRSp53 interaction is enhanced upon Arp2/3 inhibition

A shift in actin utilization upon Arp2/3 inhibition likely promotes interactions that outwardly deform the PM and polymerize F-actin locally for TNT outgrowth. Given Eps8's previously identified TNT-promoting capability (*46*), we investigated whether a specific Eps8-I-BAR interaction favours long TNT formation. We first screened Eps8's interaction with IRTKS (insulin receptor tyrosine kinase substrate) and IRSp53 based on their I-BAR domain sequence similarity (*32*) and their involvement in the formation of filopodia and microvilli (*28*, *29*, *39*, *40*). GFP-Eps8-wild type (WT) was used to immunoprecipitate endogenous IRTKS and/or IRSp53 in control and TNT-promoting conditions using CK-666 (Supplementary Fig. 5a). IRSp53 precipitated with GFP-Eps8-WT in control conditions, indicating their direct interaction in CAD cells, while IRTKS did not (Fig. 4a). To see if the interaction is affected by Arp2/3 inhibition, we treated GFP-Eps8-WT cells with CK-666. A significant increase in eluted IRSp53 was observed, whereas no effect was observed for IRTKS (Fig. 4a, b). These data indicated that interaction between Eps8 and IRSp53, but not IRTKS, would favour long TNT growth.

Using spinning disk microscopy, we then characterized the process of IRSp53- and Eps8-driven protrusions. IRSp53 and Eps8 in its bundling active form (capping defunct mutant; Eps8-ΔCAP) were separately introduced in CAD cells, and the maximum length of cell-generated protrusions was analysed before and after CK-666 addition (Fig. 4c–g). Prior to CK-666 treatment (first 30 min), IRSp53- and Eps8-ΔCAP-expressing cells were found to form lamellipodia devoid of protrusions (Fig. 4c, f and Supplementary Videos 7, 8) or shorter filopodia-like protrusions (Supplementary Fig. 6a, b and Supplementary Videos 9–12). After CK-666 addition, new IRSp53- and Eps8-positive protrusions grew two to three times longer than those found in the non-treated condition (Fig. 4d, g). Following CK-666 addition, we observed an increase of IRSp53

fluorescence at the plasma membrane (Fig. 4e, Supplementary Video 7) which then coincided with the generation and growth of IRSp53-positive dorsal protrusions, indicating a greater availability of IRSp53 to generate protrusions when branched actin pathways are inactivated.

Eps8 and IRSp53 co-expression increases the formation of functional TNTs

Together the above data suggest that Eps8 and IRSp53 specifically drive long protrusion formation and that their interaction is enhanced upon Arp2/3 inhibition. To further explore this hypothesis, we tested the effect of Eps8 and IRSp53 co-expression on TNT formation and their ability to transfer vesicles (donor-acceptor assay). Stable co-expression of GFP-Eps8-ΔCAP and IRSp53-mCherry led to a doubling in the percentage of TNT-connected cells on *D*15 micropatterns (20.8%) compared to the GFP:mCherry control cells (10.3%) (Fig. 5a, b). Notably, TNTs found in Eps8-ΔCAP:IRSp53 cells were positive for both proteins all along their length (Fig. 5a, inset iii). Furthermore, vesicle transfer from Eps8-ΔCAP:IRSp53 donors to EBFP-H2B acceptors also increased (Fig. 5c, d), while secretion-based transfer remained unchanged (Supplementary Fig. 7). As a control we overexpressed IRTKS (Supplementary Fig. 5b) and showed it had no positive impact on the percentage of TNT-connected cells (Supplementary Fig. 5c) nor on the transfer of vesicles (Supplementary Fig. 5d). Similarly, the co-expression of IRTKS with Eps8-WT and Eps8-ΔCAP showed a significant decrease in the percentage of TNT-connected cells (Supplementary Fig. 5e, f). Interestingly, the addition of CK-666 to Eps8-ΔCAP:IRSp53 cells had no further enhancement on the percentage of TNT-connected cells nor on vesicle transfer as compared to control GFP:mCherry cells (Fig. 5b, d), suggesting that the overexpression of Eps8 with IRSp53 may already saturate the cellular ability for TNTs to form.

Eps8 is removed from pathways associated with filament turnover upon Arp2/3 inhibition

To analyse the actin-centric pathways through which Eps8 and IRSp53 function, GFP-Eps8-WT or IRSp53-GFP were utilized as bait proteins in a whole-cell GFP-trap pull-down and the interactomes were assessed against appropriately-treated cytosolic GFP-expressing cells (negative controls) to identify protein hits (Supplementary Fig. 8a). In the Eps8-WT pull-down, we identified 36 proteins (out of 145) (Supplementary Fig. 8b), and the online Search Tool for Recurring Instances of Neighbouring Genes (STRING) database (*54*) was used to generate association networks where individual proteins were grouped into actin-based modules (Fig. 6a). As expected, in control conditions Eps8 preferentially interacts with IRSp53 (Baiap2), while no other I-BAR proteins were identified. Consistent with Eps8's role in membrane trafficking, several Rab-related proteins were observed, e.g., Rab5 (*55*). In addition, our analysis revealed novel hits in Eps8's interactome. We observed enrichment of Arp2/3 complex proteins (Arpc1b, Arpc3, Arpc5, Arpc5l and Actr3b). We also noted proteins directly affecting F-actin dynamics and organization, including: (1) severing proteins (gelsolin (Gsn), advillin (Avil) and flightless 1 (Flii) (*56*)) and phosphatases (Slingshot homology 1 and 2 (Ssh1 and Ssh2)) that activate cofilin (*57*); (2) pointed-end capping proteins (tropomodulins 2 and 3 (Tmod2 and Tmod3)) (*58*); (3) the bundling protein eplin (Lima 1) (*59*); and (4) coronin 2b (Coro2b) that disassembles actin branches (*60*). Finally, we observed significant pull-down of myosin-II complex proteins, consisting of both light (Myl6, Myl12a/b) and heavy (Myh10, Myh11) chain proteins, unconventional myosin motors (Myo5a/b, Myo6), and membrane-actin linkers (Myo1b/c).

After CK-666 treatment, 23 actin-related proteins were identified (out of 166), with several overlapping hits compared to the non-treated case (Fig. 6b and Supplementary Fig. 8b). Direct comparison of all the proteins in the two conditions showed changes in Eps8's interactome. Arpc5 disappeared upon treatment, while other Arp2/3 complex proteins had a fold change decrease tendency (Fig. 6c). Furthermore, we saw a clear change in proteins that are involved in actin assembly/disassembly. Avil and Ssh1 were lost (only found in the non-treated sample), while a greater enrichment of actin (Actb) and the Cdc42-effector proteins Cdc42ep1 (MSE55) and Cdc42bpa (MRCKα), which promote long extensions in fibroblasts (*61*) and deactivate cofilin through LIM kinase activation (*62*), respectively, were present in the CK-666-treated sample (Fig. 6c). Gene ontological (GO) analysis (Supplementary Fig. 8d, e) showed relative decreases in GO biological processes associated with the Arp2/3 complex, actin filament severing and capping, the negative regulation of actin filament polymerization, and vesicle-mediated transport; no relative changes were observed for pointed-end capping and F-actin bundle assembly. Together these data reveal a novel ability for Eps8 to switch its association with different proteins when branched actin networks are inhibited.

IRSp53 acts as a converging platform for actin-based processes

Our data show that IRSp53 cooperates with Eps8 to facilitate processes that lead to protrusions obtaining lengths characteristic of TNTs. How these proteins coordinate with other F-actin regulators (e.g., polymerases) in this process is unclear. Therefore, we analysed IRSp53's interactome and identified 34 and 50 actin-related protein hits in non-treated and CK-666-treated conditions, respectively (Supplementary Fig. 9a, b). From these hits, direct comparison of non-treated versus treated samples showed no significant difference (Fig. 7a) and a STRING-generated network (Fig. 7b) shows IRSp53 has an enlarged interactome as compared to Eps8. Like with Eps8, we found IRSp53 interfaces with the Arp2/3 complex and associates with proteins such as Shank3, Drebrin (Dbn1) and Lamellipodin (Raph1) that sculpt branched networks in dendritic spines and lamellipodia (*63*, *64*). However, far more WAVE and WASP proteins were observed for IRSp53 (11 proteins) as compared to Eps8 (Wasf1 only). Unlike Eps8's interactome, F-actin polymerases like the formin delphilin (Grid2ip), and those known to bind IRSp53 via SH3-mediated interactions (*28*, *34*), like Vasp and Enah, were identified. IRSp53's greater link to polymerization processes appears consistent with the observation that more actin isoforms (Actb, Actc1, Actg1, Actl6a) as well as profilin (Pfn1) were present as compared to Eps8 (Fig. 6). Furthermore, bundling proteins such as espin (Espn) (*65*) and fascin (Fscn1) were noted. Overall, these data show IRSp53 establishes a stable, multivalent interaction profile necessary to converge and promote processes affecting F-actin polymerization; however, we did not observe major changes following CK-666 treatment suggesting that Eps8's interaction with IRSp53 (which is increased upon Arp2/3 inhibition) switches the system towards longer actin filament formation necessary for TNTs.

Discussion

TNTs were identified as long, actin-supported protrusions mediating direct cargo transfer between distant cells (*7*, *8*). This transfer function in different physiological and pathological contexts (*5*, *9*, *12–15*, *18–22*, *24*, *25*) is a key difference between TNTs and filopodia (*5*). While actin is ubiquitously found in TNTs, how cells develop protrusions spanning greater distances than

311 filopodia has remained unclear, and is a remarkable feat considering any TNT must rely on the
312 polymerization of cytoskeletal elements far from the cell soma where globular actin (G-actin) is at
313 a higher effective concentration. In this work we sought to address how actin-based structures,
314 such as TNTs, are able to achieve the lengths necessary for connecting remote cells for
315 communication and whether this process relies on unique cellular machinery.
316
317 We showed that TNT formation occurs at distances significantly higher than the average length of
318 filopodia (Fig. 1), and that Arp2/3 inhibition favours both TNT formation (Fig. 2c) and actin
319 polymerization over longer distances in nanotubes mechanically pulled from cells (Fig. 3). This
320 indicates that TNTs result from a balance between linear and branched actin networks (Fig. 2 and
321 Supplementary Fig. 4). These results bear similarity to reports in yeast, and in fibroblasts and
322 macrophages, where the inhibition of Arp2/3, or the knockout of Arpc2, promoted formin-driven
323 cable assembly (*66*), stress fibres and filopodia (*67*, *68*), suggesting different actin networks are in
324 homeostasis and compete for the same pool of polymerizable G-actin (*69*). As a filopodium's
325 steady-state length is limited by the establishment of a G-actin concentration gradient between the
326 base and the barbed ends at the protrusion tip (*27*, *70*), the formation of longer filaments here for
327 TNTs could in part result from an increase in G-actin levels upon Arp2/3 inhibition.
328
329 Using Eps8 as an F-actin bundling protein shown to enhance TNTs (*46*) we identified a preferential
330 interaction with the I-BAR protein IRSp53 in CAD cells (Fig. 4a) that promoted functional TNTs
331 capable of vesicle transfer (Fig. 5), likely through a combined effect that promotes F-actin
332 bundling and stabilizes the nanotube's inherent curvatures. We found that Arp2/3 activity serves
333 as an appreciable sink for the availability of Eps8 and IRSp53 (Fig. 6 and Fig. 7). Notably, Eps8
334 associates with Arpc1b and Arpc5L isoform-specific Arp2/3 complexes recently described as
335 having higher branching activity (*71*). Eps8's interaction with Arp2/3 is likely direct given the
336 scarcity of WAVE/WASP proteins observed in our pull-down, and that diminished pull-down of
337 complex proteins and loss of Arpc5–which tethers Arp2 and Arp3 to the mother filament for
338 daughter filament branching (*72*)–was observed upon CK-666 treatment. This contrasts IRSp53's
339 SH3 domain-mediated (*37*) pull-down of far more WAVE/WASP proteins that were unaffected
340 by CK-666 treatment. Such a scenario in which different pathways compete for reactants is
341 equivalent to a mass action dependency and is a general concept controlling receptor tyrosine
342 kinase signalling (*73*) to cytoskeletal network sizes (*74*, *75*). Here, the reduced availability of Eps8
343 and IRSp53 when involved in branched networks diminishes their ability to drive outward
344 extension of long, linear F-actin. Indeed, upon Arp2/3 inhibition, an Eps8-IRSp53 interaction was
345 enhanced (Fig. 4a, b), existing Eps8- and IRSp53-positive protrusions further extended (Fig. 4f, g
346 and Supplementary Fig. 6) and IRSp53 even re-localized to the plasma membrane driving new
347 protrusion formation and extension (Fig. 4c, e). This also explains, for example, why IRSp53
348 overexpression alone partially inhibited the formation of functional TNTs in CAD cells (*46*), as a
349 new steady-state favouring actin branching was likely promoted, an effect which is amplified if
350 needed TNT-factors like Eps8 are limited within the cell.
351
352 Our results show a segregation between respective areas from where lamellipodia and TNTs
353 emerge (Fig. 2 and Supplementary Fig. 3) suggesting spatial segregation of different actin
354 networks is needed to form TNTs. While our study substantiates the role that competing networks
355 have on the propensity for TNTs to form, regulation of protein availability and distribution to
356 different pathways is needed. One possibility could involve 14-3-3 phospho-binding proteins

(identified in IRSp53's interactome, Fig. 7) which "clamp" IRSp53 in an inactive state (*76*, *77*), thus preventing its membrane binding, partner associations (e.g., Eps8) and hence its downstream control of F-actin polymerization (*38*); however, CK-666 treatment showed no change in 14-3-3 protein pull-down in IRSp53's interactome. More likely, is through Eps8's novel ability to switch its protein and pathway associations when Arp2/3 activity is attenuated that results in linear actin growth at longer distances (Fig. 3) and promotes TNTs (Fig. 5). As observed in Eps8's interactome changes (Fig. 6), regulation of F-actin severing could be achieved through: (1) diminished filament binding of barbed-end capping and actin-severing proteins (loss of Gsn, Avil and Flii); and (2) reinforcement of processes inactivating cofilin, for example, through the loss of cofilin-activating Slingshot phosphatases, and more LIM kinase activity and effectors (Cdc42ep1, Cdc42bpa) to deactivate cofilin. Proteins such as coronins (e.g., Coro2b identified in Eps8's interactome, Fig. 6) directly dissociate Arp2/3 at branching points leading to network disassembly (*60*, *78*) and would thus modify the frictional coupling of the actin bundle within the TNT to the cortex (*51*), diminishing retrograde flows and thus permit more growth. Similarly, the inhibition of myosin II-mediated contractility elongated microvilli through retrograde flow reduction (*79*). Thus, by attenuating processes that inhibit growth, the balance is shifted to processes that promote growth via Eps8- and IRSp53-mediated interactions to directly influence F-actin polymerization and bundling needed for TNTs. Our experimental work therefore reinforces *in vitro* reconstitution and theoretical work describing the control of F-actin network sizes through a polymerase to capping protein balance (*75*, *80*). Finally, such a biphasic behaviour for Eps8 is analogous with reports showing dendritic versus linear network antagonism is dependent upon profilin (*81*), since WASP (*82*), formins (*83*) and Mena/VASP (*67*, *81*) all contain profilin-binding sequences, and via the binding of tropomodulins to specific tropomyosin-decorated actin filaments (*58*).

Altogether, our study shows that the formation of TNTs depends upon common protein players and a balance between G-actin and accessory protein utilization in branched versus linear actin networks. When competing Arp2/3 networks are inhibited, this increases the availability of proteins like Eps8 and IRSp53 to exert their functions that positively lead to the extension and organization of F-actin while limiting pathways that lead to filament turnover and disassembly. While further studies are needed to elucidate the details of how Arp2/3 networks are spatially separated and disassembled, and how severing proteins are controlled to thus favour TNT growth, our work reinforces a general principle for actin network control for cellular protrusions where simple shifts in the balance between processes that inhibit growth versus those that promote growth dictate protrusion length scales.

403 # Materials and Methods

404 ## Cell culture

405 Mouse neuronal Cath.a-differentiated (CAD) cells were used in this study and were a gift from
406 Hubert Laude (Institut National de la Recherche Agronomique, Jouy-en-Josas, France). CAD cells
407 were cultured in Gibco Opti-MEM + GlutaMAX (Invitrogen) supplemented with 10% fetal bovine
408 serum (FBS; EuroBio) and 1% penicillin/streptomycin (100 u/mL final concentration; Thermo
409 Fisher Scientific). Cells were cultured at 37°C in a humidified 5% CO_2 atmosphere. Cells were
410 routinely monitored for mycoplasma contamination and found to be negative.
411

412 ## Drug treatments

413 Drugs used in this study include the Arp2/3 complex inhibitor CK-666 (*48*) and the formin agonist
414 IMM-01 (*49*) and were purchased from Sigma-Aldrich. For drug treatments prior to
415 immunoprecipitation experiments, we used 50–70% confluent CAD cells that were treated with
416 50 μM CK-666 for 1 hr. In the case of overnight drug treatments for TNT counting and co-culture
417 experiments, cells first adhered for 4–6 hr and were then treated with 50 μM CK-666 or 1 μM
418 IMM-01 for 16−18 hr. For optical tweezer experiments pre-attached cells were pre-treated for 1
419 hr with 50 μM CK-666. Control samples were treated with an equivalent amount of DMSO which
420 did not exceed 0.001% v/v.
421

422 ## Plasmids and lentiviral constructs

423 IRSp53-EGFP, IRTKS-EGFP, IRSp53-mCherry and IRTKS-mCherry were a kind gift from Pekka
424 Lappalainen (University of Helsinki, Finland) and have been described elsewhere (*32*). GFP-Eps8-
425 WT and the capping-deficient mutant GFP-Eps8-ΔCAP were a kind gift from Giorgio Scita
426 (Istituto FIRC di Oncologia Molecolare, Italy) and have been described elsewhere (*45*). tdTomato-
427 F-tractin and EGFP-F-tractin were a gift from Evelyne Coudrier (Institut Curie, France). Cytosolic
428 GFP (pEGFP-N1) and mCherry (pmCherry-N1) vectors were purchased from Clontech. H2B-
429 mCherry was a gift from Robert Benezra (Addgene plasmid #20972) and H2B-EBFP was a gift
430 from Michael Davidson (Addgene plasmid #55243).
431

432 For co-expression studies, gene inserts from GFP-Eps8-WT, GFP-Eps8-ΔCAP and IRSp53-
433 mCherry were PCR amplified using PrimeSTAR GXL DNA Polymerase (Takara Bio) and the
434 amplicons were extracted from a 1% agarose gel (Monarch Gel Extraction Kit, NEB). Inserts were
435 then cloned into a pCDH1 lentiviral vector, cut at EcoR1 and BamH1 restriction sites, using In-
436 Fusion HD Cloning Plus (Takara Bio). Short Gly/Ser linkers were added between GFP and Eps8,
437 and between IRSp53 and mCherry. Primers used in the cloning strategy include: EGFP-Xho1
438 forward (5′-GATTCTAGAGCTAGCGAATTCGCCACCATGGTGAGCA AGG-3′); EGFP-
439 linker-Xho1 reverse (5′-CTCGAGGCTAGCGCTCCCACTCCCGCTTCC
440 CTTGTACAGCTCGTCCATGCC-3′); Linker-mEps8 forward (5′-GTGGGAGCGCTAGCC
441 TCGAGATGAATGGTCATATGTCTAACCGCTC-3′); mEps8 reverse (5′-ATCCTTCGC
442 GGCCGCGGATCCTCAGTGGCTGCTCCCTTC-3′); IRSp53 forward (5′-GATTCTAGAGC
443 TAGCGAATTCGCCACCATGTCTCTGTCTCGCTCAGAGG-3′); IRSp53-linker reverse (5′-
444 CCGCTTCCGCTGTTTAAACGTCTTCCAGCCAGGGTGCG-3′); linker-mCherry forward (5′-
445 CGTTTAAACAGCGGAAGCGGGAGTGGGAGCGTGAGCAAGGGCGAG GAG-3′);
446 mCherry reverse (5′-TCCTTCGCGGCCGCGGATCCCTACTTGTACAGCTCGT CCATGC-3′).

447
448 **Transient transfection and stable lentiviral transduction**

449 Plasmid transfections were performed using Lipofectamine 2000 (Thermo Fisher Scientific)
450 according to the manufacturer's protocol. DNA:Lipofectamine 2000 complexes at a ratio of 1:3
451 (µg:µL) were added in serum-free Opti-MEM media on cells plated in 6-well plates (70%
452 confluency) and were incubated for 6 hr before removal. Transfection efficiency was verified 24
453 hr post-transfection and transfected cells were used for further experiments.
454
455 Lentiviral particles (LVs) were produced in HEK 293T cells cultured in Dulbecco's Modified
456 Eagle's Medium (Thermo Fisher Scientific), supplemented with 10% FBS (EuroBio) and 1%
457 penicillin/streptomycin (100 u/mL final concentration; Thermo Fisher Scientific) at 37°C in 5%
458 CO_2 humidified incubators. Cells were plated the day before transfection in T75 flasks (approx. 2
459 million) to achieve a 50–70% confluency the next day. Plasmids coding lentiviral components,
460 pCMVR8.74 (Gag-Pol-Hiv1) and pMDG2 (VSV-G), and the plasmid of interest at a ratio of 4:1:4
461 (µg), respectively, were transfected using FuGENE HD Transfection reagent (Promega) according
462 to the manufacturer's protocol. After 48 hr, LVs were concentrated using LentiX-Concentrator
463 (Takara Bio) and the pellet was resuspended up to 1 mL in serum-free Opti-MEM. CAD cells were
464 plated the day before infection in 6-well plates (approx. 100,000 cells) to achieve a 50–70%
465 confluency the next day. Cells were sequentially transduced with 100 µL of the desired LVs, each
466 for 24 hr. After transduction, co-expressing cells were treated with 2 µg/mL puromycin for 3 days.
467 Double-positive cells were sorted using a BD FACSAriaIII cell sorter (BD Biosciences).
468
469 **Surface micropatterning**

470 Micropatterning on glass coverslips was performed using an adapted method based Azioune et al.
471 (*84*). Round glass coverslips (25 mm, No. 1.5, Marienfeld) were sequentially cleaned in a bath
472 sonicator with 70% ethanol for 10 min and 2% Hellmanex (Hellma Analytics) for 20–30 min at
473 30°C, and then in 1 M KOH for 20 min; copious rinsing using ultra-pure water (resistivity >18
474 MΩ·cm) from a Milli-Q Advantage A-10 purification system (EMD Millipore) was performed
475 after each step. The coverslips were then dried under a stream of nitrogen and then plasma
476 activated (Harrick Plasma) for 5 min and then functionalized overnight in a 3% v/v solution of (3-
477 aminopropyl)trimethoxysilane (APTMS) in acidified methanol (5% v/v acetic acid). Following
478 aminosilanization, coverslips were briefly rinsed with 70% ethanol and then annealed in a 120°C
479 oven for 1 hr. Individual coverslips were then placed on a 60–70 µL drop of a 100 mg/mL solution
480 of mPEG-succinimidyl valerate (MW 5000, Laysan Bio) dissolved in 0.1 M $NaHCO_3$, pH 8.5 and
481 left to react overnight in a humified environment to prevent evaporation. The following day, PEG-
482 coated coverslips were rinsed in ultra-pure water and stored dry in a desiccator until they were
483 used for deep-UV micropatterning.
484
485 Custom micropattern designs were drawn in CleWin (WieWeb) and the chrome-quartz
486 photomasks were manufactured at Delta Mask (Enschede, NL). The PEG-coated coverslips were
487 held in contact with the photomask using a 2.5 µL drop of water (providing an estimated spacing
488 of 5 µm), and the photomask was placed 5 cm away (~10 mW/cm^2) from the low-pressure mercury
489 lamps (Heraeus Noblelight GmbH, NIQ 60/35 XL) housed within a UV box (UVO Cleaner,
490 Jelight); coverslips were then exposed for 5 min to deep UV light (< 200 nm) through the
491 photomask, burning exposed regions of the PEG layer to create the desired pattern on the coverslip.
492 Subsequently, to allow for stronger covalent binding of fibronectin to the patterned areas, *N*-

493 hydroxysulfosuccinimide (sulfo-NHS)/1-Ethyl-3-(3-dimethylaminopropyl)carbodiimide (EDC)
494 chemistry for amine coupling of proteins to the surface was employed. Sulfo-NHS and EDC were
495 dissolved in 0.1 M MES, 0.5 M NaCl, pH 6.0 at a concentration of 6 and 124 μM, respectively,
496 and the patterned sides of the coverslips were incubated with the sulfo-NHS/EDC solution for 30
497 min. Coverslips were then rinsed with ultra-pure water, and then incubated for 1 hr with a
498 fibronectin (FN; Bovine plasma, Sigma-Aldrich) solution having a total concentration of 35 μg/mL
499 (dissolved in 0.1 M $NaHCO_3$, pH 8.5). The FN solution was a mixture of unlabeled and dye-labeled
500 FN, where for example, fluorescent FN typically comprised 15% of the total FN concentration.
501 The micropatterned surfaces were stored at 4°C in PBS containing 1% penicillin/streptomycin
502 until used for cell seeding and typically used within one week.
503
504 **Fluorescent fibronectin**

505 Rhodamine-labelled FN was purchased from Cytoskeleton. Labelling of FN with Alexa Fluor 405
506 succinimidyl ester (Thermo Fisher Scientific) was performed in house. Briefly, lyophilized FN
507 (Bovine plasma, Sigma-Aldrich) was dissolved in PBS and dialyzed overnight against PBS to
508 remove free amines. The dialyzed FN solution was then labelled at a dye to protein ratio of 70:1
509 (mol:mol) for 1 hr at room temperature (RT) and in the dark to protect the reaction from light.
510 Extensive dialysis against PBS was then performed to remove free Alexa Fluor dye. The labelled
511 FN was concentrated using Amicon Ultra centrifugal filters (Merck), and aliquoted and stored at -
512 80°C before use. The labelling efficiency for Alexa 405 FN was determined to be 30.
513
514
515 **Characterization and analysis of cell adherence on micropatterns**

516 Reflection interference contrast microscopy (RICM) was performed on an inverted Eclipse Ti-E
517 inverted microscope (Nikon) equipped with an Antiflex 63X 1.25 NA oil immersion objective
518 (Zeiss Plan-Neofluar) and a Moment sCMOS camera (Teledyne Photometrics). Light from a
519 mercury-vapor arc lamp was bandpass filtered (546.1/10 nm, Melles Griot) and then directed
520 towards a filter cube containing a 50/50 beam splitter and two crossed polarizers prior to entering
521 the objective. An aliquot of suspended CAD cells (~20,000 cells) was added on top of a
522 micropatterned substrate mounted on a Chemlide CMB 35 mm magnetic chamber (Quorum
523 Technologies). Acquisition was controlled through MetaMorph and brightfield and RICM images
524 were acquired every 60 sec over 5 hr to capture as cells begin to adhere and spread on the
525 micropatterns. A reference fluorescence image of the FN micropatterns was taken at the first
526 timepoint only. RICM images were variance filtered in ImageJ/Fiji to highlight the contour of the
527 cell as the surrounding background exhibited low signal variance. Ten variance-filtered images
528 were then used as a training dataset in Weka for automatic segmentation of the contour of adhered
529 cells. Segmented images were binarized and the area was determined in ImageJ/Fiji through time.
530
531 **Tracking cell confinement on micropatterns**

532 Brightfield and fluorescence imaging was performed on an inverted Eclipse Ti-E or Ti2 inverted
533 microscope (Nikon) equipped with either a CSU-X1 or a CSU-W1 spinning disk confocal scanning
534 unit (Yokogawa), a fibre-coupled Coherent OBIS laser illumination system (405/488/561/640
535 nm), a 40X 1.15 NA objective (CFI Apochromat LWD Lambda S, Nikon), and a Prime 95B
536 sCMOS camera (Teledyne Photometrics). CAD cells were first pre-adhered for 1 hr to the
537 micropatterns and then imaged every 5 min over 18 hr using MetaMorph or NIS-Elements (Nikon)

538 for instrumental control. Reference fluorescence images of the FN micropatterns were taken at the
539 first timepoint only. Cells in the brightfield images were segmented from the background using an
540 Ilastik-trained model resultant from a four-image training dataset. Resulting binarized images were
541 then inputted into TrackMate to track an individual cell's centre-of-mass, with respect to the centre
542 of the cell's micropattern, through the acquisition. Tracks were overlaid on images using "Track
543 Manager" in Icy.
544
545 **Bead preparation for nanotube pulling experiments**

546 Streptavidin-coated polystyrene beads (3 µm in diameter, SVP-30-5, 0.5% w/v, Spherotech) were
547 washed three times in a 10X volume of PBS and recovered by centrifugation (12,000 rpm, 5 min).
548 Beads were then resuspended in PBS to a concentration of 0.05% w/v, and an appropriate amount
549 of a 1 mg mL^{-1} biotin-conjugated concanavalin A (ConA) solution (C2272, Sigma-Aldrich) was
550 added to the bead suspension assuming a binding capacity of 10 µg ConA per mg of beads. The
551 mixture was incubated overnight at 4°C on a tabletop shaker. ConA-coated beads were rinsed three
552 times according to the steps above and finally resuspended in PBS to a concentration of 0.5% w/v.
553 ConA-beads were stored at 4°C and generally usable up to one month.
554
555 **Nanotube pulling experiments**

556 A home-built optical tweezer (OT) coupled to an inverted Eclipse Ti C1 Plus confocal microscope
557 (Nikon) was used as previously described (*38*). Briefly, a 3-watt 1064 nm Ytterbium fiber laser
558 (IPG Photonics) was expanded through a Keplerian telescope and directed towards the back
559 aperture of a 100X 1.45 NA oil immersion objective (Nikon CFI Plan Apochromat Lambda). The
560 viscous drag method, including Faxen's correction for calibration near surfaces, was used to
561 determine the OT trap stiffness which averaged 60 pN μm^{-1}. Displacements of the bead from the
562 fixed trap centre were recorded on a CCD camera (Marlin F-046B, Allied-Vision) at a frame rate
563 of 20 fps and videos were later analysed using a custom MATLAB (Mathworks) script based on
564 the "imfindcircles" function to determine the bead's centre of mass. Forces were calculated from
565 the bead positions according to the equation $F = \kappa \cdot \Delta x$ where κ is the trap stiffness and Δx is the
566 displacement of the bead from its initial reference position determined before nanotube pulling. A
567 Nano-LP100 piezo-driven stage (MadCityLabs) was used for lateral XY movements on the setup.
568 A temperature and CO_2 controllable stage-top incubator (STXG-WELSX, Tokai Hit) maintained
569 cells at 37°C in a humidified, 5% CO_2 atmosphere during experimentation.
570
571 The day before experimentation, CAD cells expressing EGFP-F-Tractin were seeded on
572 micropatterned coverslips in which the fibronectin patches were separated at a distance of 50 µm
573 to ensure cells were well-separated for micromanipulation. One-hour prior to experimentation the
574 phenol-containing culture medium was removed, cells were rinsed with PBS, and exchanged for a
575 phenol-free Opti-MEM medium containing: 10% FCS, ProLong™ Live Antifade Reagent
576 (Invitrogen) at a 1:75 dilution, 2 mg mL^{-1} β-Casein (>98% pure, from bovine milk, Sigma-Aldrich)
577 for surface passivation, and 50 µM CK-666 (or the equivalent volume of DMSO for control
578 experiments). The cells were taken to the optical tweezer setup and labeled with Cell Mask™ Deep
579 Red plasma membrane stain (Invitrogen) at a 1:2000 dilution for 10 min, and ConA-coated beads
580 were added (1:50–1:100 dilution). Using a custom LabVIEW (National Instruments) program to
581 control the piezo stage, membrane nanotubes were pulled by trapping an isolated floating bead,
582 bringing it into contact with the cell for a short period of time (<10 sec), and then moving the cell
583 away from the bead in the X direction. Confocal image acquisition using 488 nm (Coherent) and

584 642 nm (Melles Griot) lasers were controlled with the EZ-C1 software (Nikon). Fluorescence was
585 bandpass filtered (ET525/50, ET665, Chroma) and detected using τ-SPAD single-photon
586 avalanche diodes (PicoQuant) that were controlled by the SymPhoTime 64 software (PicoQuant).
587 Images encompassing the nanotube and some of the cell body (typically 1024 x 512 pixels, 5X
588 zoom) were gathered every 30 sec after pulling.
589
590 **Quantification of actin profiles in pulled nanotubes**

591 Image analysis was performed using custom written macros in ImageJ/Fiji. Images for the
592 membrane and actin channels were first background subtracted, and the actin channel was then
593 normalized by the average cytosolic signal measured within the cell interior to account for
594 differences in F-Tractin expression. From the membrane channel image, the nanotube's cross-
595 section was fit to a Gaussian function to determine the ±2σ width of the Gaussian profile. Using
596 the line selection tool, a line was drawn starting within the cytosol, intersecting through the plasma
597 membrane and then following all along the length of the nanotube; the width of the line was set to
598 the measured ±2σ width in order to encompass the entire thickness of the nanotube. Profiles were
599 then extracted and the actin intensity plotted as a function of the length of the nanotube X, where
600 $X = 0$ was defined as the position of the max intensity value found within the plasma membrane
601 rim near the base of the nanotube. For curve averaging, profiles were interpolated in MATLAB to
602 obtain vectors of all the same length.
603
604 **GFP-trap immunoprecipitation**

605 GFP-trap was performed using anti-GFP nanobody-coated agarose beads (Chromotek) and was
606 carried out following the supplier's recommendations. Briefly, 1.2 million CAD cells expressing
607 the GFP-tagged "bait" protein of interest were plated in 100 mm dishes. The subsequent day the
608 cells were briefly washed with PBS after drug treatment, and then scraped and centrifuged at 500
609 g for 3 min at 4°C. The supernatant was gently removed, and lysis buffer was added (4–5 volumes
610 of lysis buffer for 1 volume of cell pellet). The lysis buffer consisted of 50 mM Tris, 1% Triton,
611 300 mM NaCl, 5 mM $MgCl_2$, cOmplete™ Mini EDTA-free Protease Inhibitor Cocktail (Merck)
612 at pH 7.4. The cells were lysed on ice for 30 min, after which the lysate was cleared at 14,000 rpm
613 for 30 min at 4°C. The cell lysate protein concentration was quantified using a Bradford protein
614 assay (Bio-Rad). Agarose beads were rinsed and equilibrated in PBS, recovered by centrifugation
615 and then resuspended in PBS +/+ (1:1 ratio). After which 20 µL of resuspended beads were added
616 per immunoprecipitation (IP) sample (300 µg of total protein) along with 300 µL of dilution buffer
617 (10 mM Tris, 150 mM NaCl, 0.5% Triton, pH 7.5). The IP mixture was diluted with sterile distilled
618 water, so that the final Triton concentration did not exceed 0.5% v/v, and was then incubated for
619 1 hr at 4°C with gentle agitation to bind proteins. Three washes of 3 min each were carried out
620 with wash buffer (10 mM Tris, 150 mM NaCl, 0.5% Triton, pH 7.5). Finally, bound proteins were
621 eluted with 20 µL of 2X Laemmli sample buffer (Bio-Rad) and the sample was subsequently
622 denatured at 100°C for 5 min.
623
624 **SDS-PAGE and Western Blot analysis**

625 SDS-PAGE was performed in 1X MOPS buffer (Sigma-Aldrich) on Criterion 4–12% precast gels
626 (Bio-Rad). Wells were loaded with the total eluent volume from the IP samples, containing 300
627 µg of protein, whereas 10% (30 µg) was loaded for the lysate control samples (input). The
628 migration was done at 120 mV for approximately 2 hr. Proteins were transferred (100 V, 1 hr) onto

629 PVDF (polyvinylidene difluoride) membranes (GE Healthcare Life Sciences) using 1X
630 Tris/Glycine buffer (in-house 50X solution containing 250 mM Tris and 1920 mM Glycine). After
631 transfer, the membrane was blocked using 5% non-fat milk in 0.1% TBS-T (1X Tris-Buffered
632 Saline, 0.1% Tween 20, Bio-Rad) for 1 hr at RT. Primary antibodies were added at the appropriate
633 dilution, and membranes were incubated overnight at 4°C under agitation. Primary antibodies used
634 include: rabbit polyclonal anti-GFP (1:4000, A-6455, Thermo Fisher Scientific), rabbit polyclonal
635 anti-IRSp53 (1:1000, HPA023310, Sigma-Aldrich), rabbit polyclonal anti-IRTKS (1:2000,
636 HPA019484, Sigma-Aldrich), and mouse monoclonal anti-α tubulin (1:5000, T5168, Sigma-
637 Aldrich) as a loading control. Membranes were washed three times in TBS-T for 10 min and mouse
638 and rabbit horseradish peroxidase (HRP)-tagged secondary antibodies were added to the
639 membrane at a 1:5000 dilution in 5% milk, for 1 hr at RT. Membranes were revealed using
640 Amersham ECL Prime (Cytiva) chemiluminescent detection reagent and imaged using an
641 ImageQuant LAS 500TM imager (GE Healthcare Life Sciences).
642
643 To quantify relative changes in band intensities (measured as an average value), regions of interest
644 of the same size were drawn in ImageJ/Fiji to encompass the appropriate GFP band of the bait
645 protein (indicates the amount of eluted bait protein), the band of the prey protein, and background
646 values adjacent to the measured bands. Background-corrected band intensities were finally
647 normalized by taking the prey band divided by the bait band.
648
649 **TNT quantification**

650 On micropatterns: CAD cells were mechanically detached in serum-free Opti-MEM containing
651 0.5 mM EGTA (to prevent cadherin-mediated cell clumping), strained through a 40 µm nylon cell
652 strainer (Corning) and diluted to a concentration of 175,000 cells/mL using Opti-MEM containing
653 10% FBS to better ensure singularized cells. Micropatterned coverslips were generally attached to
654 the bottom of open 35 mm dishes (P35G-1.5-20-C, MatTek) using silicon grease (Dow Corning),
655 and 60,000 cells were seeded within the volume defined by the 20 mm dish opening. Otherwise,
656 micropatterned coverslips were placed in 6-well plates and 250,000 cells were used for seeding in
657 this case. After 4–6 hr of adherence, unattached cells were then removed manually using a pipette
658 by gently rinsing with PBS. Cells were then cultured 16−18 hr overnight prior to a two-step
659 fixation and dye staining.
660
661 Cells were fixed with 2% paraformaldehyde (16% PFA aqueous solution, methanol free, EM
662 grade, Electron Micorscopy Sciences), 0.05% glutaraldehyde (25% GA aqueous solution, Grade
663 I, Sigma-Aldrich), 0.2 M HEPES (1 M HEPES, Gibco) in PBS for 20 min at 37°C, followed by a
664 second fixation in 4% PFA, 0.2 M HEPES in PBS for 20 min at 37°C. Following fixation, cells
665 were quenched in 50 mM NH_4Cl for 10–30 min at RT and carefully washed in PBS prior to dye
666 labelling. Alexa Fluor 647 phalloidin or Rhodamine phalloidin (1:50–1:200 dilution in PBS, 30
667 min incubation in the dark at RT; Thermo Fisher Scientific) was used for F-actin staining, WGA
668 Alexa Fluor 488 conjugate (1:300 dilution in PBS, 20 min incubation in the dark at RT; Thermo
669 Fisher Scientific) was used to stain the plasma membrane, and 4',6-diamidino-2-phenylindole
670 (DAPI) (1:1000 dilution, 2 min incubation in the dark at RT) was used to stain the nuclei. Between
671 staining, samples were washed with PBS. Finally, samples were mounted/sealed using Aqua-
672 Poly/Mount (Polysciences) or Mowiol 4-88 (Sigma-Aldrich) and left to polymerize overnight in
673 the dark.
674

675 Samples were imaged using a 40X 1.3 NA oil immersion objective (Zeiss Plan Apo) on an inverted
676 confocal microscope (Zeiss LSM 700) equipped with 405/488/561/640 nm lasers and controlled
677 by the ZEN software. The whole cellular volume, typically 12 µm in thickness, was imaged by
678 acquiring 0.4 µm-thick slices. Images were analyzed in the Icy software using the "Manual TNT
679 annotation" plug-in (http://icy.bioimageanalysis.org/plugin/manual-tnt-annotation/) for manual
680 identification and numeration of cells connected by TNTs. Connections between cells on
681 neighbouring micropatterns were annotated as TNTs if the following criteria were met: (i) they
682 were thin (diameter < 800 nm), (ii) membranous and F-actin positive, (iii) did not contact the
683 substrate and thus would be found in the middle and upper stacks, and (iv) were continuous along
684 their length without obvious breaks (e.g., tip-to-tip bound filopodia) to directly link the cell bodies
685 of the connected cells. The percent of TNT-connected cells on micropatterns was obtained by
686 counting the TNT-connected cells and dividing by the number of nearest-neighbour cell-occupied
687 micropatterns (i.e., isolated cell-occupied micropatterns were excluded since nearest-neighbour
688 micropatterns are unoccupied and thus incapable of having a TNT spanning between
689 micropatterns).
690
691 In normal cell culture: In Supplementary Figs 4 and 5, 220,000 cells were plated into 35 mm Ibidi
692 µ-dishes (Ibidi), cultured 18 hr overnight and then fixed, stained and imaged similarly to what was
693 described above for the micropatterned samples. The percent of TNT-connected cells was obtained
694 by counting the TNT-connected cells in an image and dividing by the total number of cells present
695 in the field of view.
696
697 **Manual single-cell analysis of TNT origin**

698 Wild-type CAD cells plated on D*15* micropatterns (see TNT quantification on micropatterns, Fig.
699 2) were classified into either a mixed cell phenotype (exhibiting hairy/filopodial and
700 lamellipodial/ruffled characteristics) or a lamellipodia-only phenotype. Then, the immediate
701 cellular vicinity from which the TNT was originating was categorised. TNTs were categorised as
702 emanating from a filopodia-rich region, directly from a lamellipodia/ruffle region, or spatially
703 separated above a lamellipodia/ruffle region.
704
705 **Quantification of vesicle transfer by co-culture assays**

706 By confocal microscopy: Vesicle transfer assays such as those in Supplementary Fig. 2 and Fig. 5
707 were performed on *D*15 micropatterns, while IMM-01 drug-treated co-cultures were performed in
708 35 mm Ibidi µ-dishes (Supplementary Fig. 4). Donor cells were stained with DiD (Thermo Fisher
709 Scientific; 1:3000 dilution in culture media for 30 min in the dark at 37°C) to visualize vesicles,
710 whereas cells expressing a fluorescently tagged histone 2b (H2B) fusion protein were used as
711 acceptor cells. Predominately, H2B-EBFP-transfected CAD cells were used as an acceptor cell
712 population unless otherwise stated. Donors and acceptors were co-cultured overnight (16−18 hr)
713 at a 1:1 ratio; the total amount of cells plated in Ibidi µ-dishes was 200,000, while the number of
714 cells plated on *D*15 micropatterns (placed in 6-well plates) was 250,000. In parallel, supernatant
715 controls were performed in Ibidi µ-dishes to measure secretion-based vesicle transfer. Here, equal
716 amounts of donor and acceptor cells (100,000 for Ibidi-based co-cultures and 125,000 for
717 micropattern-based co-cultures) were separately cultured. After 16−18 hr, the conditioned media
718 of the donors was collected, briefly centrifuged (1,000 rpm, 4 min) to remove dead cells, and then
719 exchanged for the media of the acceptor cell sample. The acceptors cells were then cultured for
720 another overnight incubation with the conditioned media. All samples were fixed, stained and

721 imaged according to the protocol described above for TNT quantification. The Icy software was
722 used to annotate acceptor cells with and without internalized DiD-positive vesicles. The percent
723 of total transfer was assessed by quantifying the number of acceptor cells containing donor-derived
724 DiD-vesicles and dividing it by the total number of acceptor cells analysed across the acquired
725 images for a given sample.
726
727 By flow cytometry: In Supplementary Fig. 5d, CAD cells expressing IRTKS-EGFP where stained
728 with DiD (donor population) and cultured at a 1:1 ratio (300,000 total cells) with H2B-mCherry
729 expressing CAD cells (acceptor population) in 6-well plates. In parallel, co-cultures using EGFP
730 expressing donor cells were used as controls. After an overnight co-culture (16−18 hr), cells were
731 mechanically detached and washed briefly with a dilute trypsin solution (0.03% w/v trypsin in
732 PBS) to remove non-internalized vesicles attached on the cell exterior. Cells were passed through
733 a 40 µm nylon cell strainer to separate cell aggregates and fixed in 2% PFA. Flow cytometry data
734 was acquired with a FACSymphony A5 flow cytometer (BD Biosciences). GFP, mCherry and DiD
735 fluorescence were analysed at excitation wavelengths of 488, 561 and 647 nm, respectively. Ten
736 thousand events were acquired for each condition and data was analysed using FlowJo (BD
737 Biosciences). The percent of total transfer was calculated by dividing the number of double
738 positive cells (H2B-mCherry acceptor cells containing donor-derived DiD-vesicles) with the total
739 number of analysed H2B-mCherry acceptor cells (Q2/Q1). Two biological repeats were conducted
740 with each condition done in triplicate.
741
742 **Time-lapse microscopy of protrusion formation**

743 CAD cells at 50–70% confluency were co-transfected with IRSp53-EGFP and tdTomato-F-tractin
744 or GFP-Eps8-ΔCAP and tdTomato-F-tractin according to the transfection protocol above. Six
745 hours prior to the acquisition, 220,000 of the co-transfected cells were plated in 35 mm dishes
746 (Ibidi), or 250,000 cells were plated on 40 µm fibronectin micropatterns placed in 6-well plates
747 (Supplementary Fig. 6, Example 3). Samples were mounted on a Chemlide CMB 35 mm magnetic
748 chamber (Quorum Technologies). Time-lapse imaging was performed on an Eclipse Ti-E inverted
749 microscope (Nikon) equipped with a CSU-X1 spinning disk confocal scanning unit (Yokogawa),
750 a 60X 1.4 NA oil immersion objective (Nikon Plan Apo VC), a fiber-coupled Coherent OBIS laser
751 illumination system (405/488/561/640 nm), and Prime 95B sCMOS cameras (Teledyne
752 Photometrics) for single or dual camera mode acquisition. Acqusition was controlled by
753 MetaMorph. Two positions with z-stack slices (0.6 µm thickness) covering the 12 µm cell volume
754 were acquired at a 1-min interval over 90 min (except when imaging IRSp53 recruitment at the
755 membrane which was imaged with a 30-sec interval). Cells were imaged 30 min prior to flowing
756 in CK-666 at a final concentration of 50 µM, that was subsequently imaged for 60 min. A
757 humidified 37°C and a 5% CO_2 environment was maintained in a Life Imaging Services Gmbh
758 enclosure.
759
760 **Filopodia quantification and length measurements**

761 For fixed conditions (Fig. 1g), filopodia were quantified using the automated analysis pipeline
762 developed by Bagonis et al. (*85*). Maximum intensity projection images of filopodia (both surface-
763 and non-attached) were created and the cell bodies were manually segmented for filopodia
764 detection using phalloidin staining. When needed, Hyugens (Scientific Volume Imaging) was used
765 for image deconvolution to improve filopodia detection in samples having weak actin
766 fluorescence.

767 For time-lapse imaging (Fig. 4d, g), maximum intensity projection images were created in
768 ImageJ/Fiji. In the first 30 min of imaging (control condition prior to CK-666 addition), a
769 protrusion containing actin (as F-tractin) and the protein of interest was followed and when it
770 reached its maximum length (e.g., just before retraction), its length was manually measured from
771 its base to the tip. The same procedure was performed after CK-666 treatment, with the difference
772 being that the imaging duration was increased to 60 min in order to sample length changes in
773 manually tracked protrusions.
774
775 **Fluorescence profile measurements**

776 The intensity of IRSp53 at the membrane (Fig. 4e) before and after the addition of CK-666 was
777 analysed in ImageJ/Fiji ("Plot Profile" plugin) by drawing a straight line (10 µm long)
778 perpendicular to the cell edge. The middle of the line was positioned directly at the boundary of
779 cell edge and the background such that individual curves could be properly aligned and overlaid.
780
781 **Proteomic analysis by mass spectrometry**

782 Sample preparation: CAD cells were plated in 100 mm dishes (800,000 cells) the day before
783 transfection. Following a 24-hr transfection, GFP-Eps8-WT or IRSp53-EGFP cells, along with
784 cytosolic GFP-expressing cells, were treated in parallel either with DMSO or with 50 µM CK-666
785 for 1 hr. After washing and lysing the cells, samples were processed for GFP-trap
786 immunoprecipitation (described above). After protein binding, two 3-min washes were done in
787 lysis buffer followed by three 3-min washes in the dilution buffer prior to on-bead digestion and
788 mass spectrometry (MS) analysis. Three independent preparations were performed for Eps8, while
789 five independent preparations were performed for IRSp53.
790
791 On-bead digestion followed by LC-MS/MS analysis: Digestion was performed strictly as
792 described by Chromotek. Briefly, beads were resuspended in digestion buffer (50 mM Tris-HCl
793 pH 7.5, 2 M urea, 1 mM DTT and 5 µg/µl of trypsin (Promega)) for 3 min at 30°C. Supernatants
794 were transferred to new vials and beads were washed twice using 50 mM Tris-HCl pH 7.5, 2 M
795 urea and 5 mM iodoacetamide buffer. All washes were pooled and incubated at 32°C for overnight
796 digestion in the dark. Peptides were purified using a standard C18-based clean-up protocol using
797 a Bravo AssayMap device (Agilent). LC-MS/MS analysis of digested peptides was performed on
798 an Orbitrap Q Exactive Plus mass spectrometer (Thermo Fisher Scientific) coupled to an EASY-
799 nLC 1200 (Thermo Fisher Scientific). A home-made C18 column was used for peptide separation
800 and consisted of a 30 cm nano-HPLC capillary column (75 µm inner diameter) filled with 1.9 µm
801 Reprosil-Pur Basic C18-HD resin (Dr. Maisch HPLC GmbH) that terminated with a silica
802 PicoTip® emitter tip (New Objective). The column was equilibrated and peptides were loaded in
803 100% solvent A (H_2O, 0.1% formic acid (FA)) at 900 bars. Peptides were eluted at 300 nL min^{-1}
804 using a linear gradient of solvent B (acetonitrile (ACN), 0.1 % FA) from 2% to 35% during 55
805 min, 35% to 60% during 10 min, and 60% to 90% during 5 min (total chromatographic run was
806 80 min including a high ACN step and a column regeneration step). Mass spectra were acquired
807 in the data-dependent acquisition mode with the XCalibur 2.2 software (Thermo Fisher Scientific).
808 Automatic switching between MS and MS/MS scans was performed to select the 10 most abundant
809 precursor ions (top10 method) from the survey scan for higher-energy collision dissociation
810 (HCD) peptide fragmentation. Survey MS scans were acquired at a resolution of 70,000 (at m/z
811 400) with a target value of 3×10^6 ions and was limited in range from 400 to 1700 m/z. HCD
812 peptide fragmentation was performed with a normalized collision energy (NCE) set at 27%.

813 Intensity threshold for ion selection was set at 1×10^6 ions with a charge-state exclusion of z = 1
814 and z > 7. The MS/MS spectra were acquired at a resolution of 17,500 (at m/z 400). Isolation
815 window was set at 1.6 Th. Dynamic exclusion was employed within 30 s.
816
817 Protein identification and quantification: MS Data were searched using MaxQuant (version
818 1.6.6.0) employing the Andromeda search engine (*86*) against a reference *Mus musculus* proteome
819 (55,470 entries; downloaded from Uniprot June 1, 2021). The following search parameters were
820 applied: carbamidomethylation of cysteines was set as a fixed modification, while oxidation of
821 methionine and protein N-terminal acetylation were set as variable modifications. The mass
822 tolerances in MS and MS/MS were set to 5 ppm and 20 ppm, respectively. Maximum peptide
823 charge was set to 7 and 5 amino acids were required as a minimum peptide length. At least 2
824 peptides (including 1 unique peptide) were asked to report a protein identification. A false
825 discovery rate (FDR) of 1% was set for both protein and peptide levels. Intensity-based absolute
826 quantification (iBAQ) values were generated from the sum of peak intensities of all peptides
827 corresponding to a specific protein divided by the number of observable peptides. The match
828 between runs features was allowed for biological replicate only.
829
830 Statistical analysis: Proteins identified in the reverse and contaminant databases and proteins "only
831 identified by site" were first removed from the analysis. Remaining proteins with at least 2 peptides
832 were kept for further analysis and the associated peptide intensities were summed and log
833 transformed ($\log_2$). Summed intensity values were normalized by median centering within
834 conditions (*normalizeD* function of the R package *DAPAR*) (*87*). Proteins without any iBAQ value
835 in a condition, while present in another, have been considered as proteins quantitatively present in
836 a condition and absent in the other. Next, missing values were imputed using the *impute.mle*
837 function of the R package *imp4p* (*88*). Proteins with a fold-change inferior to 1.5 (i.e., $\log_2(FC) <$
838 0.58) are considered not significantly differentially abundant between conditions. Statistical
839 testing of proteins with a FC superior to 1.5 was conducted using a limma t-test thanks to the R
840 package *limma* (*89*). An adaptive Benjamini-Hochberg procedure was applied on the resulting p-
841 values thanks to the *adjust.p* function of the R package *cp4p* (*90*) using the robust method
842 described in (*91*) to estimate the proportion of true null hypotheses among the set of statistical
843 tests. The proteins associated to an adjusted P-value inferior to an FDR level of 1% have been
844 considered as significantly differentially abundant proteins. Thus, proteins of interest are therefore
845 those considered to be present in one condition and absent in another, and those proteins identified
846 based on pairwise comparison of intensities according to the adjusted P-value and FC thresholds.
847
848 **Bioinformatic analysis**

849 UniProt identifiers/accession numbers of the proteins of interest (specifically those related to the
850 actin cytoskeleton) were inputted into the online Search Tool for Recurring Instances of
851 Neighbouring Genes (STRING) database (*54*) to generate an interaction network visualized using
852 Cytoscape. Medium confidence (minimum score, 0.4) interactions were sourced from databases,
853 experiments, co-expression, neighborhood and gene fusion evidence. The proteins in the network
854 were grouped manually according to their function and the networks were then exported as .svg
855 files for color coding in Adobe Illustrator for easier visualization. Gene Ontology (GO) analysis
856 of biological processes was performed using PANTHER 17.0, employing Fisher's Exact test with
857 a false discovery rate (FDR) correction. The whole *Mus musculus* gene database was used as a
858 reference list. Output parameters for a given GO term include: 1) the protein count in the input; 2)

a reference count (Ref cout) for the total number of proteins in the mouse database assigned to a given GO term; 3) the fold enrichment value (observed/expected) which is determined from the protein count divided by the number of proteins expected to be annotated in a randomly generated network of the same size; and 4) the FDR that measures the significance of the fold enrichment.

Statistical analysis

Statistical analysis was performed in GraphPad Prism. $P < 0.05$ was considered statistically significant and all P values are indicated in the figures. The specific statistical tests performed, the number of independent experiments and the total number of samples analysed are indicated in the figure captions.

Data availability

The mass spectrometry proteomics data have been deposited to the ProteomeXchange Consortium via the PRIDE (*92*) partner repository with the dataset identifier PXD035976. All data needed to evaluate the conclusions in the paper are present in the paper and/or the Supplementary Materials.

Acknowledgements

We thank all laboratory members for insightful discussions, particularly Christel Brou, Stéphanie Lebrenton and Feng-Ching Tsai for their critical reading of the manuscript. We are also grateful for the administrative support provided by Reine Bouyssie (Membrane Traffic and Pathogenesis Unit, Institut Pasteur). We additionally thank Juliette Wu, a former intern, for help in some early immunoprecipitation experiments, and Fanny Tabarin-Cayrac (Institut Curie) and Pierre-Henri Commere (Institut Pasteur) for cell sorting assistance. The authors greatly acknowledge experimental support from the Institut Pasteur Unit of Technology and Service for Cytometry and Biomarkers (UTechS CB), and the Photonic BioImaging platform (UTechS PBI) which is a member of the France BioImaging infrastructure (FBI) network that is supported by the French Agence Nationale de la Recherche (ANR-10-INBS-04). J.M.H. was supported by a Pasteur Foundation Postdoctoral Fellowship and N.L. was supported by the Sorbonne Université (doctoral grant number 3210/2018). P.B. acknowledges support from the Centre National de la Recherche Scientifique (CNRS Défi Instrumentation aux limites 2018), and is a member of the CNRS consortium Approches Quantitatives du Vivant (AQV), Labex Cell(n)Scale (ANR-11-LABX0038) and Paris Sciences et Lettres (ANR-10-IDEX-0001-02). C.Z. acknowledges support from the Equipe Fondation Recherche Médicale (FRM EQU202103012692). This work was supported by grants from the Université Paris Sciences et Lettres-QLife Institute (ANR-17-CONV-0005 Q-LIFE) and the Agence Nationale de la Recherche (ANR-20-CE13-0032 LiveTuneL) to P.B. and C.Z.

Contributions

J.M.H., P.B. and C.Z. conceived the study and acquired funding. J.M.H. and N.L. designed and performed experiments, analysed the resulting data, and wrote the original manuscript. T.C. performed mass spectrometry measurements and performed statistical analyses with Q.G.G under the supervision of M.M. D.C. performed IMM-01 experiments. A.B. provided molecular biology expertise, reagents and generated lentiviral constructs used in the study. S.D. provided technical

902 expertise and design assistance for the micropatterning protocol. J.M.H., N.L., P.B. and C.Z.
903 reviewed and edited the final manuscript. All authors approved the manuscript prior to submission.

904 **References**

905 1. P. Mattila, P. Lappalainen, Filopodia: molecular architecture and cellular functions. *Nat Rev*
906 *Mol Cell Biol*. **9**, 446–454 (2008).

907 2. M. C. Bischoff, S. Lieb, R. Renkawitz-Pohl, S. Bogdan, Filopodia-based contact
908 stimulation of cell migration drives tissue morphogenesis. *Nat. Commun.* **12**, 791 (2021).

909 3. A. Jacinto, W. Wood, T. Balayo, M. Turmaine, A. Martinez-Arias, P. Martin, Dynamic
910 actin-based epithelial adhesion and cell matching during Drosophila dorsal closure. *Curr.*
911 *Biol.* **10**, 1420–1426 (2000).

912 4. G. Mancinelli, L. Lamparter, G. Nosov, T. Saha, A. Pawluchin, R. Kurre, C. Rasch, M.
913 Ebrahimkutty, J. Klingauf, M. Galic, Dendrite tapering actuates a self-organizing signaling
914 circuit for stochastic filopodia initiation in neurons. *Proc. Natl. Acad. Sci.* **118** (2021),
915 doi:10.1073/pnas.2106921118.

916 5. N. Ljubojevic, J. M. Henderson, C. Zurzolo, The Ways of Actin: Why Tunneling
917 Nanotubes Are Unique Cell Protrusions. *Trends Cell Biol.* **31**, 130–142 (2021).

918 6. A. Sartori-Rupp, D. Cordero Cervantes, A. Pepe, K. Gousset, E. Delage, S. Corroyer-
919 Dulmont, C. Schmitt, J. Krijnse-Locker, C. Zurzolo, Correlative cryo-electron microscopy
920 reveals the structure of TNTs in neuronal cells. *Nat. Commun.* **10**, 342 (2019).

921 7. A. Rustom, R. Saffrich, I. Markovic, P. Walther, H.-H. Gerdes, Nanotubular Highways for
922 Intercellular Organelle Transport. *Science*. **303**, 1007–1010 (2004).

923 8. B. Önfelt, S. Nedvetzki, K. Yanagi, D. M. Davis, Cutting Edge: Membrane Nanotubes
924 Connect Immune Cells. **173**, 1511–1513 (2004).

925 9. X. Wang, M. L. Veruki, N. V. Bukoreshtliev, E. Hartveit, H.-H. Gerdes, Animal cells
926 connected by nanotubes can be electrically coupled through interposed gap-junction
927 channels. *Proc. Natl. Acad. Sci.* **107**, 17194–17199 (2010).

928 10. G. Haimovich, C. M. Ecker, M. C. Dunagin, E. Eggan, A. Raj, J. E. Gerst, R. H. Singer,
929 Intercellular mRNA trafficking via membrane nanotube-like extensions in mammalian
930 cells. *Proc. Natl. Acad. Sci.* **114**, E9873–E9882 (2017).

931 11. N. Rainy, D. Chetrit, V. Rouger, H. Vernitsky, O. Rechavi, D. Marguet, I. Goldstein, M.
932 Ehrlich, Y. Kloog, H-Ras transfers from B to T cells via tunneling nanotubes. *Cell Death*
933 *Dis.* **4**, e726 (2013).

934 12. P. D. Arkwright, F. Luchetti, J. Tour, C. Roberts, R. Ayub, A. P. Morales, J. J. Rodríguez,
935 A. Gilmore, B. Canonico, S. Papa, M. D. Esposti, Fas stimulation of T lymphocytes

936 promotes rapid intercellular exchange of death signals via membrane nanotubes. *Cell Res.*
937 **20**, 72–88 (2010).

938 13. S. Abounit, L. Bousset, F. Loria, S. Zhu, F. de Chaumont, L. Pieri, J.-C. Olivo-Marin, R.
939 Melki, C. Zurzolo, Tunneling nanotubes spread fibrillar α-synuclein by intercellular
940 trafficking of lysosomes. *EMBO J.* **35**, 2120–2138 (2016).

941 14. X. Wang, H.-H. Gerdes, Transfer of mitochondria via tunneling nanotubes rescues
942 apoptotic PC12 cells. *Cell Death Differ.* **22**, 1181–1191 (2015).

943 15. T. Saha, C. Dash, R. Jayabalan, S. Khiste, A. Kulkarni, K. Kurmi, J. Mondal, P. K.
944 Majumder, A. Bardia, H. L. Jang, S. Sengupta, Intercellular nanotubes mediate
945 mitochondrial trafficking between cancer and immune cells. *Nat. Nanotechnol.* **17**, 98–106
946 (2022).

947 16. A. Rustom, The missing link: does tunnelling nanotube-based supercellularity provide a
948 new understanding of chronic and lifestyle diseases? *Open Biol.* **6**, 160057 (2016).

949 17. C. Zurzolo, Tunneling nanotubes: Reshaping connectivity. *Curr. Opin. Cell Biol.* **71**, 139–
950 147 (2021).

951 18. L. Alarcon-Martinez, D. Villafranca-Baughman, H. Quintero, J. B. Kacerovsky, F. Dotigny,
952 K. K. Murai, A. Prat, P. Drapeau, A. Di Polo, Interpericyte tunnelling nanotubes regulate
953 neurovascular coupling. *Nature*. **585**, 91–95 (2020).

954 19. A. A. Kalargyrou, M. Basche, A. Hare, E. L. West, A. J. Smith, R. R. Ali, R. A. Pearson,
955 Nanotube-like processes facilitate material transfer between photoreceptors. *EMBO Rep.*
956 **22**, e53732 (2021).

957 20. A. Ortin-Martinez, N. E. Yan, E. L. S. Tsai, L. Comanita, A. Gurdita, N. Tachibana, Z. C.
958 Liu, S. Lu, P. Dolati, N. T. Pokrajac, A. El-Sehemy, P. E. B. Nickerson, C. Schuurmans, R.
959 Bremner, V. A. Wallace, Photoreceptor nanotubes mediate the in vivo exchange of
960 intracellular material. *EMBO J.* **40**, e107264 (2021).

961 21. S. Sisakhtnezhad, L. Khosravi, Emerging physiological and pathological implications of
962 tunneling nanotubes formation between cells. *Eur. J. Cell Biol.* **94**, 429–443 (2015).

963 22. S. Sowinski, C. Jolly, O. Berninghausen, M. A. Purbhoo, A. Chauveau, K. Köhler, S.
964 Oddos, P. Eissmann, F. M. Brodsky, C. Hopkins, B. Onfelt, Q. Sattentau, D. M. Davis,
965 Membrane nanotubes physically connect T cells over long distances presenting a novel
966 route for HIV-1 transmission. *Nat Cell Biol*. **10**, 211–9 (2008).

967 23. A. Pepe, S. Pietropaoli, M. Vos, G. Barba-Spaeth, C. Zurzolo, Tunneling nanotubes provide
968 a route for SARS-CoV-2 spreading. *Sci. Adv.* **8**, eabo0171 (2022).

969 24. H. Scheiblich, C. Dansokho, D. Mercan, S. V. Schmidt, L. Bousset, L. Wischhof, F. Eikens,
970 A. Odainic, J. Spitzer, A. Griep, S. Schwartz, D. Bano, E. Latz, R. Melki, M. T. Heneka,

971 Microglia jointly degrade fibrillar alpha-synuclein cargo by distribution through tunneling
972 nanotubes. *Cell*. **184**, 5089-5106.e21 (2021).

973 25. M. Sharma, S. Subramaniam, Rhes travels from cell to cell and transports Huntington
974 disease protein via TNT-like protrusion. *J. Cell Biol.* **218**, 1972–1993 (2019).

975 26. P. Chastagner, F. Loria, J. Y. Vargas, J. Tois, M. I Diamond, G. Okafo, C. Brou, C.
976 Zurzolo, Fate and propagation of endogenously formed Tau aggregates in neuronal cells.
977 *EMBO Mol. Med.* **12**, e12025 (2020).

978 27. A. Mogilner, B. Rubinstein, The physics of filopodial protrusion. *Biophys. J.* **89**, 782–795
979 (2005).

980 28. A. Disanza, S. Bisi, M. Winterhoff, F. Milanesi, D. S. Ushakov, D. Kast, P. Marighetti, G.
981 Romet-Lemonne, H.-M. Müller, W. Nickel, J. Linkner, D. Waterschoot, C. Ampè, S.
982 Cortellino, A. Palamidessi, R. Dominguez, M.-F. Carlier, J. Faix, G. Scita, CDC42 switches
983 IRSp53 from inhibition of actin growth to elongation by clustering of VASP. *EMBO J.* **32**,
984 2735–50 (2013).

985 29. D. Garbett, C. Sauvanet, R. Viswanatha, A. Bretscher, The tails of apical scaffolding
986 proteins EBP50 and E3KARP regulate their localization and dynamics. *Mol. Biol. Cell*. **24**,
987 3381–3392 (2013).

988 30. J. Choi, J. Ko, B. Racz, A. Burette, J.-R. Lee, S. Kim, M. Na, H. W. Lee, K. Kim, R. J.
989 Weinberg, E. Kim, Regulation of Dendritic Spine Morphogenesis by Insulin Receptor
990 Substrate 53, a Downstream Effector of Rac1 and Cdc42 Small GTPases. *J. Neurosci.* **25**,
991 869–879 (2005).

992 31. C. Prévost, H. Zhao, J. Manzi, E. Lemichez, P. Lappalainen, A. Callan-Jones, P. Bassereau,
993 IRSp53 senses negative membrane curvature and phase separates along membrane tubules.
994 *Nat. Commun.* **6**, 8529 (2015).

995 32. J. Saarikangas, H. Zhao, A. Pykäläinen, P. Laurinmäki, P. K. Mattila, P. K. J. Kinnunen, S.
996 J. Butcher, P. Lappalainen, Molecular mechanisms of membrane deformation by I-BAR
997 domain proteins. *Curr. Biol.* **19**, 95–107 (2009).

998 33. A. Disanza, S. Mantoani, M. Hertzog, S. Gerboth, E. Frittoli, A. Steffen, K. Berhoerster,
999 H.-J. Kreienkamp, F. Milanesi, P. P. D. Fiore, A. Ciliberto, T. E. B. Stradal, G. Scita,
1000 Regulation of cell shape by Cdc42 is mediated by the synergic actin-bundling activity of the
1001 Eps8–IRSp53 complex. *Nat. Cell Biol.* **8**, 1337–1347 (2006).

1002 34. F. Vaggi, A. Disanza, F. Milanesi, P. P. Di Fiore, E. Menna, M. Matteoli, N. S. Gov, G.
1003 Scita, A. Ciliberto, The Eps8/IRSp53/VASP Network Differentially Controls Actin
1004 Capping and Bundling in Filopodia Formation. *PLoS Comput. Biol.* **7**, e1002088 (2011).

1005 35. W. I. Goh, K. B. Lim, T. Sudhaharan, K. P. Sem, W. Bu, A. M. Chou, S. Ahmed, mDia1
1006 and WAVE2 Proteins Interact Directly with IRSp53 in Filopodia and Are Involved in
1007 Filopodium Formation. *J. Biol. Chem.* **287**, 4702–4714 (2012).

1008 36. K. B. Lim, W. Bu, W. I. Goh, E. Koh, S. H. Ong, T. Pawson, T. Sudhaharan, S. Ahmed,
1009 The Cdc42 Effector IRSp53 Generates Filopodia by Coupling Membrane Protrusion with
1010 Actin Dynamics. *J. Biol. Chem.* **283**, 20454–20472 (2008).

1011 37. H. Miki, H. Yamaguchi, S. Suetsugu, T. Takenawa, IRSp53 is an essential intermediate
1012 between Rac and WAVE in the regulation of membrane ruffling. *Nature*. **408**, 732–735
1013 (2000).

1014 38. F.-C. Tsai, J. M. Henderson, Z. Jarin, E. Kremneva, Y. Senju, J. Pernier, O. Mikhajlov, J.
1015 Manzi, K. Kogan, C. L. Clainche, G. A. Voth, P. Lappalainen, P. Bassereau, Activated I-
1016 BAR IRSp53 clustering controls the formation of VASP-actin-based membrane
1017 protrusions. *bioRxiv* (2022), , doi:10.1101/2022.03.04.483020.

1018 39. M. M. Postema, N. E. Grega-Larson, A. C. Neininger, M. J. Tyska, IRTKS (BAIAP2L1)
1019 Elongates Epithelial Microvilli Using EPS8-Dependent and Independent Mechanisms.
1020 *Curr. Biol.* **28**, 2876-2888.e4 (2018).

1021 40. T. Sudhaharan, K. P. Sem, H. F. Liew, Y. H. Yu, W. I. Goh, A. M. Chou, S. Ahmed, The
1022 Rho GTPase Rif signals through IRTKS, Eps8 and WAVE2 to generate dorsal membrane
1023 ruffles and filopodia. *J. Cell Sci.* **129**, 2829–2840 (2016).

1024 41. G. Scita, J. Nordstrom, R. Carbone, P. Tenca, G. Giardina, S. Gutkind, M. Bjarnegård, C.
1025 Betsholtz, P. P. D. Fiore, EPS8 and E3B1 transduce signals from Ras to Rac. *Nature*. **401**,
1026 290 (1999).

1027 42. G. Scita, P. Tenca, L. B. Areces, A. Tocchetti, E. Frittoli, G. Giardina, I. Ponzanelli, P. Sini,
1028 M. Innocenti, P. P. Di Fiore, An effector region in Eps8 is responsible for the activation of
1029 the Rac-specific GEF activity of Sos-1 and for the proper localization of the Rac-based
1030 actin–polymerizing machine. *J. Cell Biol.* **154**, 1031–1044 (2001).

1031 43. C. Yang, T. Svitkina, Visualizing branched actin filaments in lamellipodia by electron
1032 tomography. *Nat. Cell Biol.* **13**, 1012–1013 (2011).

1033 44. A. Disanza, M.-F. Carlier, T. E. B. Stradal, D. Didry, E. Frittoli, S. Confalonieri, A. Croce,
1034 J. Wehland, P. P. Di Fiore, G. Scita, Eps8 controls actin-based motility by capping the
1035 barbed ends of actin filaments. *Nat. Cell Biol.* **6**, 1180–1188 (2004).

1036 45. M. Hertzog, F. Milanesi, L. Hazelwood, A. Disanza, H. Liu, E. Perlade, M. G. Malabarba,
1037 S. Pasqualato, A. Maiolica, S. Confalonieri, C. L. Clainche, N. Offenhauser, J. Block, K.
1038 Rottner, P. P. D. Fiore, M.-F. Carlier, N. Volkmann, D. Hanein, G. Scita, Molecular Basis
1039 for the Dual Function of Eps8 on Actin Dynamics: Bundling and Capping. *PLOS Biol.* **8**,
1040 e1000387 (2010).

1041 46. E. Delage, D. C. Cervantes, E. Pénard, C. Schmitt, S. Syan, A. Disanza, G. Scita, C.
1042 Zurzolo, Differential identity of Filopodia and Tunneling Nanotubes revealed by the
1043 opposite functions of actin regulatory complexes. *Sci. Rep.* **6**, 39632 (2016).

1044 47. N. Matejka, J. Reindl, Perspectives of cellular communication through tunneling nanotubes
1045 in cancer cells and the connection to radiation effects. *Radiat. Oncol.* **14**, 218 (2019).

1046 48. B. Hetrick, M. S. Han, L. A. Helgeson, B. J. Nolen, Small molecules CK-666 and CK-869
1047 inhibit actin-related protein 2/3 complex by blocking an activating conformational change.
1048 *Chem. Biol.* **20**, 701–712 (2013).

1049 49. L. L. Lash, B. J. Wallar, J. D. Turner, S. M. Vroegop, R. E. Kilkuskie, S. M. Kitchen-
1050 Goosen, H. E. Xu, A. S. Alberts, Small-Molecule Intramimics of Formin Autoinhibition: A
1051 New Strategy to Target the Cytoskeletal Remodeling Machinery in Cancer Cells. *Cancer*
1052 *Res.* **73**, 6793–6803 (2013).

1053 50. A. Datar, T. Bornschlögl, P. Bassereau, J. Prost, P. A. Pullarkat, Dynamics of Membrane
1054 Tethers Reveal Novel Aspects of Cytoskeleton-Membrane Interactions in Axons. *Biophys.*
1055 *J.* **108**, 489–497 (2015).

1056 51. T. Bornschlogl, S. Romero, C. L. Vestergaard, J.-F. Joanny, G. T. Van Nhieu, P. Bassereau,
1057 Filopodial retraction force is generated by cortical actin dynamics and controlled by
1058 reversible tethering at the tip. *Proc. Natl. Acad. Sci.* **110**, 18928–18933 (2013).

1059 52. B. Pontes, N. B. Viana, L. T. Salgado, M. Farina, V. M. Neto, H. M. Nussenzveig, Cell
1060 cytoskeleton and tether extraction. *Biophys. J.* **101**, 43–52 (2011).

1061 53. N. Leijnse, Y. F. Barooji, M. R. Arastoo, S. L. Sønder, B. Verhagen, L. Wullkopf, J. T.
1062 Erler, S. Semsey, J. Nylandsted, L. B. Oddershede, A. Doostmohammadi, P. M. Bendix,
1063 Filopodia rotate and coil by actively generating twist in their actin shaft. *Nat. Commun.* **13**,
1064 1636 (2022).

1065 54. D. Szklarczyk, A. L. Gable, K. C. Nastou, D. Lyon, R. Kirsch, S. Pyysalo, N. T. Doncheva,
1066 M. Legeay, T. Fang, P. Bork, L. J. Jensen, C. von Mering, The STRING database in 2021:
1067 customizable protein-protein networks, and functional characterization of user-uploaded
1068 gene/measurement sets. *Nucleic Acids Res.* **49**, D605–D612 (2021).

1069 55. L. Lanzetti, V. Rybin, M. G. Malabarba, S. Christoforidis, G. Scita, M. Zerial, P. P. Di
1070 Fiore, The Eps8 protein coordinates EGF receptor signalling through Rac and trafficking
1071 through Rab5. *Nature*. **408**, 374–377 (2000).

1072 56. S. Nag, M. Larsson, R. C. Robinson, L. D. Burtnick, Gelsolin: The tail of a molecular
1073 gymnast. *Cytoskeleton*. **70**, 360–384 (2013).

1074 57. R. Niwa, K. Nagata-Ohashi, M. Takeichi, K. Mizuno, T. Uemura, Control of Actin
1075 Reorganization by Slingshot, a Family of Phosphatases that Dephosphorylate ADF/Cofilin.
1076 *Cell*. **108**, 233–246 (2002).

1077 58. R. Kumari, Y. Jiu, P. J. Carman, S. Tojkander, K. Kogan, M. Varjosalo, P. W. Gunning, R.
1078 Dominguez, P. Lappalainen, Tropomodulins Control the Balance between Protrusive and
1079 Contractile Structures by Stabilizing Actin-Tropomyosin Filaments. *Curr. Biol. CB*. **30**,
1080 767-778.e5 (2020).

1081 59. R. S. Maul, Y. Song, K. J. Amann, S. C. Gerbin, T. D. Pollard, D. D. Chang, EPLIN
1082 regulates actin dynamics by cross-linking and stabilizing filaments. *J. Cell Biol.* **160**, 399–
1083 407 (2003).

1084 60. L. Cai, T. W. Marshall, A. C. Uetrecht, D. A. Schafer, J. E. Bear, Coronin 1B Coordinates
1085 Arp2/3 Complex and Cofilin Activities at the Leading Edge. *Cell*. **128**, 915–929 (2007).

1086 61. P. D. Burbelo, D. M. Snow, W. Bahou, S. Spiegel, MSE55, a Cdc42 effector protein,
1087 induces long cellular extensions in fibroblasts. *Proc. Natl. Acad. Sci.* **96**, 9083–9088
1088 (1999).

1089 62. T. Sumi, K. Matsumoto, A. Shibuya, T. Nakamura, Activation of LIM Kinases by
1090 Myotonic Dystrophy Kinase-related Cdc42-binding Kinase α*. *J. Biol. Chem.* **276**, 23092–
1091 23096 (2001).

1092 63. P. Hotulainen, C. C. Hoogenraad, Actin in dendritic spines: connecting dynamics to
1093 function. *J. Cell Biol.* **189**, 619–629 (2010).

1094 64. S. D. Hansen, R. D. Mullins, Lamellipodin promotes actin assembly by clustering
1095 Ena/VASP proteins and tethering them to actin filaments. *eLife*. **4**, e06585 (2015).

1096 65. G. Sekerková, P. A. Loomis, B. Changyaleket, L. Zheng, R. Eytan, B. Chen, E. Mugnaini,
1097 J. R. Bartles, Novel Espin Actin-Bundling Proteins Are Localized to Purkinje Cell
1098 Dendritic Spines and Bind the Src Homology 3 Adapter Protein Insulin Receptor Substrate
1099 p53. *J. Neurosci.* **23**, 1310–1319 (2003).

1100 66. T. A. Burke, J. R. Christensen, E. Barone, C. Suarez, V. Sirotkin, D. R. Kovar, Homeostatic
1101 Actin Cytoskeleton Networks Are Regulated by Assembly Factor Competition for
1102 Monomers. *Curr. Biol.* **24**, 579–585 (2014).

1103 67. J. D. Rotty, C. Wu, E. M. Haynes, C. Suarez, J. D. Winkelman, H. E. Johnson, J. M.
1104 Haugh, D. R. Kovar, J. E. Bear, Profilin-1 Serves as a Gatekeeper for Actin Assembly by
1105 Arp2/3-Dependent and -Independent Pathways. *Dev. Cell*. **32**, 54–67 (2015).

1106 68. J. D. Rotty, H. E. Brighton, S. L. Craig, S. B. Asokan, N. Cheng, J. P. Ting, J. E. Bear,
1107 Arp2/3 Complex Is Required for Macrophage Integrin Functions but Is Dispensable for FcR
1108 Phagocytosis and In Vivo Motility. *Dev. Cell*. **42**, 498-513.e6 (2017).

1109 69. C. Suarez, D. R. Kovar, Internetwork competition for monomers governs actin cytoskeleton
1110 organization. *Nat. Rev. Mol. Cell Biol.* **17**, 799–810 (2016).

1111 70. Y. Lan, G. A. Papoian, The Stochastic Dynamics of Filopodial Growth. *Biophys. J.* **94**,
1112 3839–3852 (2008).

1113 71. J. V. G. Abella, C. Galloni, J. Pernier, D. J. Barry, S. Kjær, M.-F. Carlier, M. Way, Isoform
1114 diversity in the Arp2/3 complex determines actin filament dynamics. *Nat. Cell Biol.* **18**, 76–
1115 86 (2016).

1116 72. I. Rouiller, X.-P. Xu, K. J. Amann, C. Egile, S. Nickell, D. Nicastro, R. Li, T. D. Pollard, N.
1117 Volkmann, D. Hanein, The structural basis of actin filament branching by the Arp2/3
1118 complex. *J. Cell Biol.* **180**, 887–895 (2008).

1119 73. C. Kiel, E. Verschueren, J.-S. Yang, L. Serrano, Integration of Protein Abundance and
1120 Structure Data Reveals Competition in the ErbB Signaling Network. *Sci. Signal.* **6**, ra109–
1121 ra109 (2013).

1122 74. M. Rank, A. Mitra, L. Reese, S. Diez, E. Frey, Limited Resources Induce Bistability in
1123 Microtubule Length Regulation. *Phys. Rev. Lett.* **120**, 148101 (2018).

1124 75. D. S. Banerjee, S. Banerjee, Emergence and maintenance of variable-length actin filaments
1125 in a limiting pool of building blocks. *Biophys. J.* (2022), doi:10.1016/j.bpj.2022.05.014.

1126 76. J. M. Robens, L. Yeow-Fong, E. Ng, C. Hall, E. Manser, Regulation of IRSp53-Dependent
1127 Filopodial Dynamics by Antagonism between 14-3-3 Binding and SH3-Mediated
1128 Localization. *Mol. Cell. Biol.* **30**, 829–844 (2010).

1129 77. D. J. Kast, R. Dominguez, IRSp53 coordinates AMPK and 14-3-3 signaling to regulate
1130 filopodia dynamics and directed cell migration. *Mol. Biol. Cell*. **30**, 1285–1297 (2019).

1131 78. S. Jansen, A. Collins, S. M. Chin, C. A. Ydenberg, J. Gelles, B. L. Goode, Single-molecule
1132 imaging of a three-component ordered actin disassembly mechanism. *Nat. Commun.* **6**,
1133 7202 (2015).

1134 79. C. R. Chinowsky, J. A. Pinette, L. M. Meenderink, K. S. Lau, M. J. Tyska, Nonmuscle
1135 myosin-2 contractility-dependent actin turnover limits the length of epithelial microvilli.
1136 *Mol. Biol. Cell*. **31**, 2803–2815 (2020).

1137 80. A. Antkowiak, A. Guillotin, M. B. Sanders, J. Colombo, R. Vincentelli, A. Michelot, Sizes
1138 of actin networks sharing a common environment are determined by the relative rates of
1139 assembly. *PLOS Biol.* **17**, e3000317 (2019).

1140 81. K. Skruber, P. V. Warp, R. Shklyarov, J. D. Thomas, M. S. Swanson, J. L. Henty-Ridilla,
1141 T.-A. Read, E. A. Vitriol, Arp2/3 and Mena/VASP Require Profilin 1 for Actin Network
1142 Assembly at the Leading Edge. *Curr. Biol.* (2020), doi:10.1016/j.cub.2020.04.085.

1143 82. P. Bieling, S. D. Hansen, O. Akin, T.-D. Li, C. C. Hayden, D. A. Fletcher, R. D. Mullins,
1144 WH2 and proline-rich domains of WASP-family proteins collaborate to accelerate actin
1145 filament elongation. *EMBO J.* **37**, 102–121 (2018).

1146 83. C. Suarez, R. T. Carroll, T. A. Burke, J. R. Christensen, A. J. Bestul, J. A. Sees, M. L.
1147 James, V. Sirotkin, D. R. Kovar, Profilin Regulates F-Actin Network Homeostasis by
1148 Favoring Formin over Arp2/3 Complex. *Dev. Cell*. **32**, 43–53 (2015).

1149 84. A. Azioune, M. Storch, M. Bornens, M. Théry, M. Piel, Simple and rapid process for single
1150 cell micro-patterning. *Lab. Chip*. **9**, 1640 (2009).

1151 85. M. M. Bagonis, L. Fusco, O. Pertz, G. Danuser, Automated profiling of growth cone
1152 heterogeneity defines relations between morphology and motility. *J. Cell Biol.* **218**, 350–
1153 379 (2018).

1154 86. S. Tyanova, T. Temu, J. Cox, The MaxQuant computational platform for mass
1155 spectrometry-based shotgun proteomics. *Nat. Protoc.* **11**, 2301–2319 (2016).

1156 87. S. Wieczorek, F. Combes, C. Lazar, Q. Giai Gianetto, L. Gatto, A. Dorffer, A.-M. Hesse,
1157 Y. Couté, M. Ferro, C. Bruley, T. Burger, DAPAR & ProStaR: software to perform
1158 statistical analyses in quantitative discovery proteomics. *Bioinforma. Oxf. Engl.* **33**, 135–
1159 136 (2017).

1160 88. Q. G. Gianetto, S. Wieczorek, Y. Couté, T. Burger, A peptide-level multiple imputation
1161 strategy accounting for the different natures of missing values in proteomics data (2020), p.
1162 2020.05.29.122770, , doi:10.1101/2020.05.29.122770.

1163 89. G. K. Smyth, Linear models and empirical bayes methods for assessing differential
1164 expression in microarray experiments. *Stat. Appl. Genet. Mol. Biol.* **3**, Article3 (2004).

1165 90. S. Pounds, C. Cheng, Robust estimation of the false discovery rate. *Bioinforma. Oxf. Engl.*
1166 **22**, 1979–1987 (2006).

1167 91. Q. Giai Gianetto, F. Combes, C. Ramus, C. Bruley, Y. Couté, T. Burger, Calibration plot
1168 for proteomics: A graphical tool to visually check the assumptions underlying FDR control
1169 in quantitative experiments. *Proteomics*. **16**, 29–32 (2016).

1170 92. Y. Perez-Riverol, J. Bai, C. Bandla, D. García-Seisdedos, S. Hewapathirana, S.
1171 Kamatchinathan, D. J. Kundu, A. Prakash, A. Frericks-Zipper, M. Eisenacher, M. Walzer,
1172 S. Wang, A. Brazma, J. A. Vizcaíno, The PRIDE database resources in 2022: a hub for
1173 mass spectrometry-based proteomics evidences. *Nucleic Acids Res.* **50**, D543–D552 (2022).

1174

1175

1176

1177

1178

1179

1180

Figures

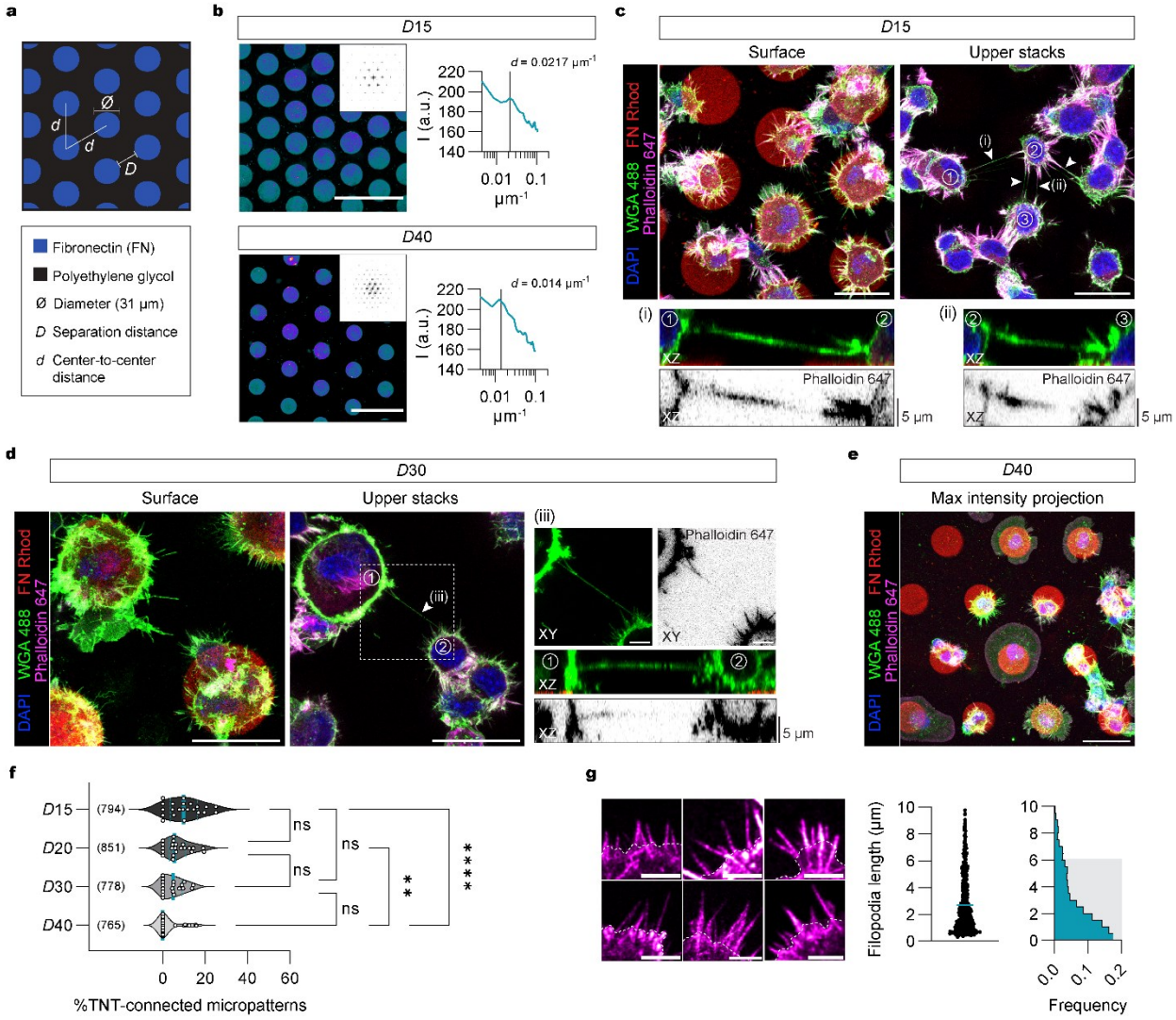

Fig. 1: TNTs connect neighbouring CAD cells across varying distances.
(a) Cartoon depicting fibronectin (FN) patterns produced as a hexagonal array of circles (diameter of 31 µm) with edge-to-edge separation distances (*D*) of 15, 20, 30 and 40 µm were tuned along the center-to-center distance (*d*) between circles. **(b)** Left: Representative fluorescent images of FN micropatterns spaced by 15 and 40 µm with their respective calculated fast Fourier transform (FFT) images (upper right insets). Right: Corresponding radial profiles determined from the FFT images plotted as a function of the spatial frequency (μm^{-1}). Solid lines in the radial profile plots indicate the expected center-to-center *d* spacing between circular patterns and line up nicely with peaks in the measured profile, indicating high fidelity in the manufacturing process. **(c, d)** Representative surface and upper stack maximum intensity projections of CAD cells plated on 15 and 30 µm FN micropatterns. TNTs connecting cells on two different micropatterns are annotated with a white arrowhead. Subpanels (i, ii, iii) show zoom-ins and XZ projections through the axis

of the indicated TNTs. **(e)** Representative maximum intensity projection of CAD cells plated on 40 μm FN micropatterns showing no TNTs between cells. **(f)** Violin plot of the percentage of TNT-connected micropatterns for *D*15, *D*20, *D*30 and *D*40 micropatterns. The median percentage of TNT-connected micropatterns (teal solid lines in the plot) on *D*15, *D*20, *D*30 and *D*40 micropatterns is 9.8%, 5.5%, 4.8%, and 0%, respectively; quartiles are annotated with dotted teal lines. Each data point corresponds to a quantified image in which on average approximately 30 cell-occupied micropatterns were within the acquired field of view; data was pooled from three experiments. The total number of individual micropatterns quantified per condition is indicated in parentheses. Statistical analysis was performed using a Kruskal Wallis test with Dunn's multiple comparison test. ns = non-significant for $P > 0.9999$; **, $P = 0.0074$; ****, $P < 0.0001$. **(g)** Left: Representative images of CAD cell filopodia (magenta, Phalloidin-Alexa Flour 647). Cell body edges are marked with a dotted white line. Right: Dot plot of individual filopodia lengths (18 cells, $n = 546$ filopodia) and the corresponding histogram showing that 90% of the population (shaded gray region) had lengths that were less than 6 μm. Scale bars: (**b**) 100 μm; (**c - e**) 30 μm, Subpanels, 5 μm; (**g**) 5 μm.

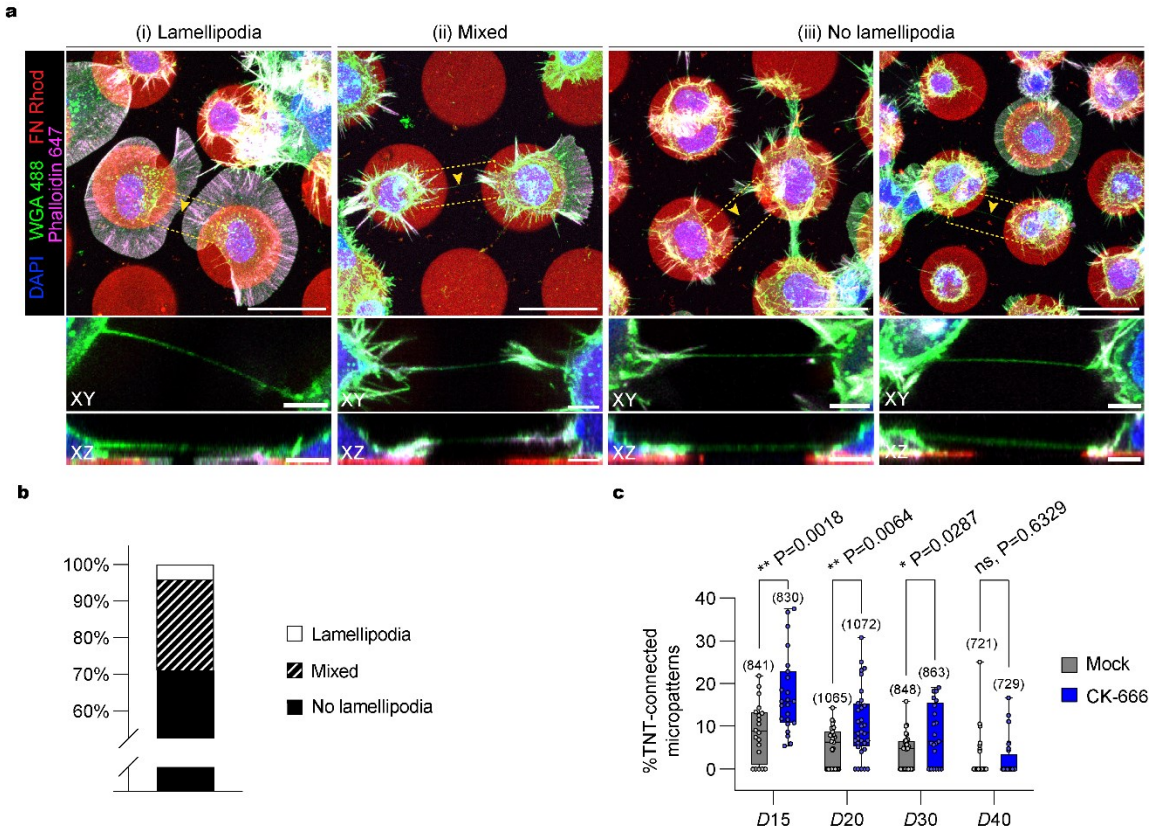

Fig. 2: TNT prevalence negatively correlates with Arp2/3 activity.
(**a, b**) TNT-connected cells characteristically lack lamellipodial features. (**a**) Representative maximum intensity projection images of cells with different morphologies that are connected by TNTs. TNTs can be formed (i) between two cells forming only lamellipodia, (ii) between two cells showing a mix of phenotypes (e.g., one of the connected cells displays only (or partial) lamellipodia while the other connected cell shows no lamellipodia), or (iii) between two non-lamellipodia cells displaying a higher density of peripheral protrusions. Dashed yellow boxes correspond to subpanels below each image that show zoom-ins and XZ projections of TNTs that were made through the axis of the connection. Yellow arrowheads directly point to the TNT. (**b**) Bar graph showing the characterization of TNTs between cells of different morphologies plated on *D*15 micropatterns (n = 97 TNTs). Lamellipodia, 4.1%; Mixed, 24.7%; and No Lamellipodia, 71.1%. (**c**) Whisker box plot showing the percentage of TNT-connected micropatterns for *D*15, *D*20, *D*30 and *D*40 micropatterns in cells treated with 50 µM CK-666 as compared to the mock condition (DMSO vehicle control). Mock vs. CK-666 average values were 8.8 ± 1.5% vs. 17.6 ± 1.9% for *D*15 micropatterns, 5.0 ± 0.8% vs. 10.6 ± 1.4% for *D*20 micropatterns, 4.0 ± 0.8% vs. 8.3 ± 1.5% for *D*30 micropatterns, and 2.0 ± 0.9% vs. 2.3 ± 0.8% for *D*40 micropatterns (mean ± SEM). Each data point corresponds to a quantified image in which on average approximately 30 cell-occupied micropatterns were within the acquired field of view; data was pooled from three experiments. The total number of individual micropatterns quantified in each condition is indicated above each box. The data was analysed using an unpaired Mann-Whitney test. Scale bars, 30 µm; Subpanels, 5 µm.

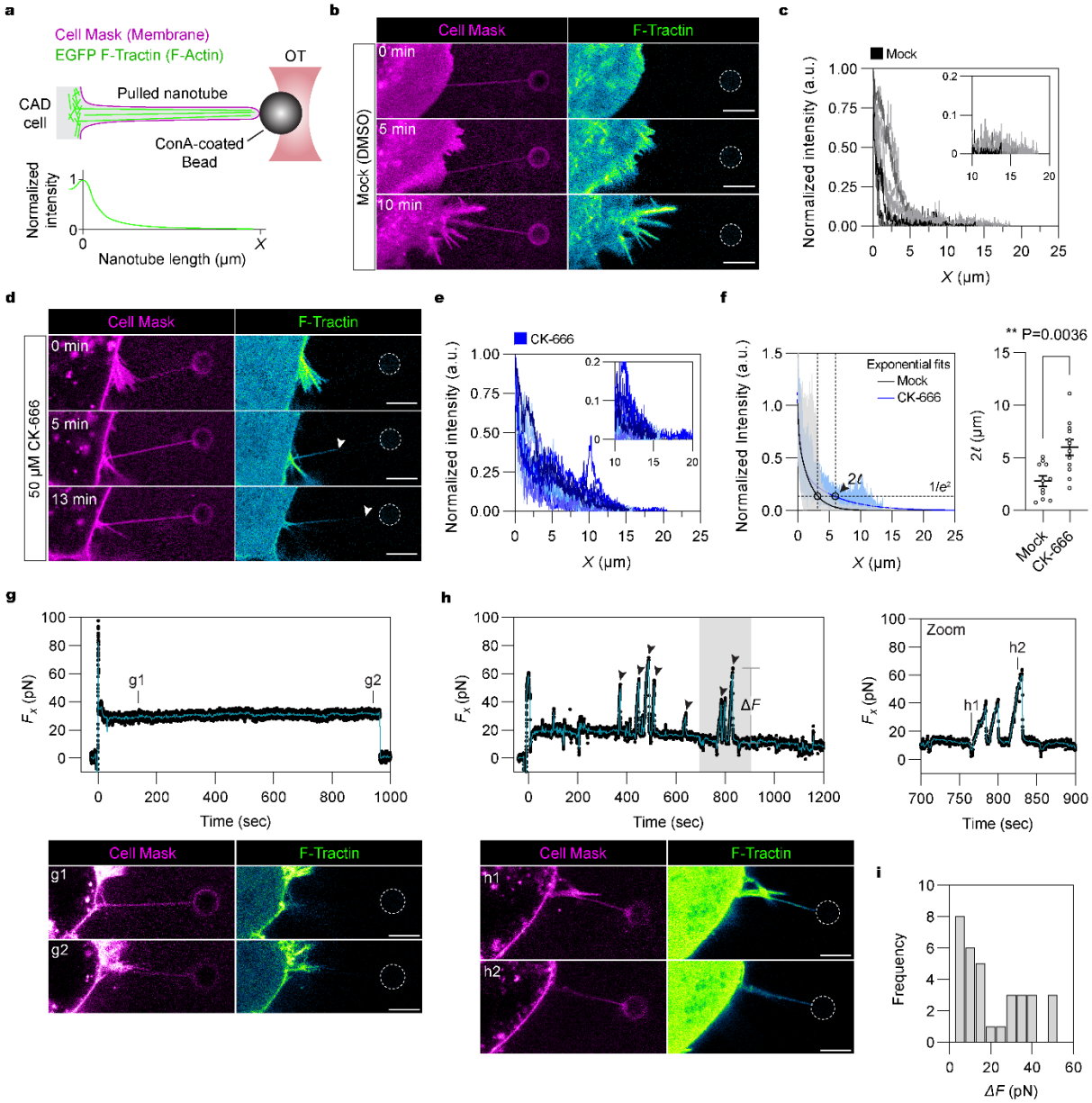

Fig. 3: Inhibition of branched actin formation results in greater F-actin development in pulled nanotubes.

(**a**) Experimental setup for pulling membrane nanotubes using a concanavalin A (Con-A)-coated bead (~3 μm in diameter) trapped in an optical tweezer (OT). CAD cells stably expressing the small F-actin-binding peptide F-tractin fused to EGFP (green) were exogenously labelled with the lipophilic Cell Mask™ Deep Red plasma membrane stain (magenta). Intensity profiles of the F-actin fluorescence were measured along the nanotube axis and plotted against the nanotube length. (**b, d**) Representative time-lapse images of a nanotube pulled from a DMSO-treated (mock control) (Supplementary Video 5) and a CK-666-treated cell (Supplementary Video 6). White arrowheads annotate the progression of actin development within the nanotube in **d**. (**c, e**) Plot of actin profiles within pulled nanotubes for mock- and CK-666-treated cells. Insets show a magnified view at the

tube extremity to better highlight the greater presence of F-actin in the CK-666 condition as compared to the mock condition. Mock condition, 11 tubes; CK-666 condition, 12 tubes. (**f**) Left: Exponential fits to the actin intensity profiles were performed to determine a characteristic decay length (2ℓ) at which the initial intensity at $X = 0$ decays to a value of $1/e^2$. For visualization purposes of the analysis, exponential fits are shown for the mean actin profiles computed from the individual plots presented in **e** and **f**. Upper and lower limits of the intensity range are shaded. Right: Dot plot of the characteristic decay lengths (2ℓ) for mock- and CK-666-treated cells. Data is represented as the mean ± SEM. Mock (11 tubes), 2.78 ± 0.50; CK-666 (12 tubes), 5.80 ± 0.73. Statistical analysis was performed using an unpaired Mann-Whitney test. (**g**) Top: Force plot of a pulled nanotube from a mock-treated cell showing no F-actin development. Solid teal line, 10-point moving average curve. Bottom: Associated images of the indicated time points (g1, g2). (**h**) Top: Force plot of a pulled nanotube from a CK-666-treated cell showing F-actin development spanning the entire nanotube length. Peaks in the force plot (black arrowheads), with magnitudes of ΔF, arise when retrograde flows outcompete actin polymerization (at the nanotube tip) causing bead displacement towards the cell body (recorded as a positive rise in the force in the lab frame). Solid teal line, 10-point moving average curve. Shaded grey region corresponds to a magnified view on the right. Bottom: Associated images of the indicated time points (h1, h2). (**i**) Histogram of the force peak magnitudes (ΔF). Sample size, 33 peaks. The trapped bead is annotated by a dotted white circle when not clearly visible. Scale bars, 5 μm.

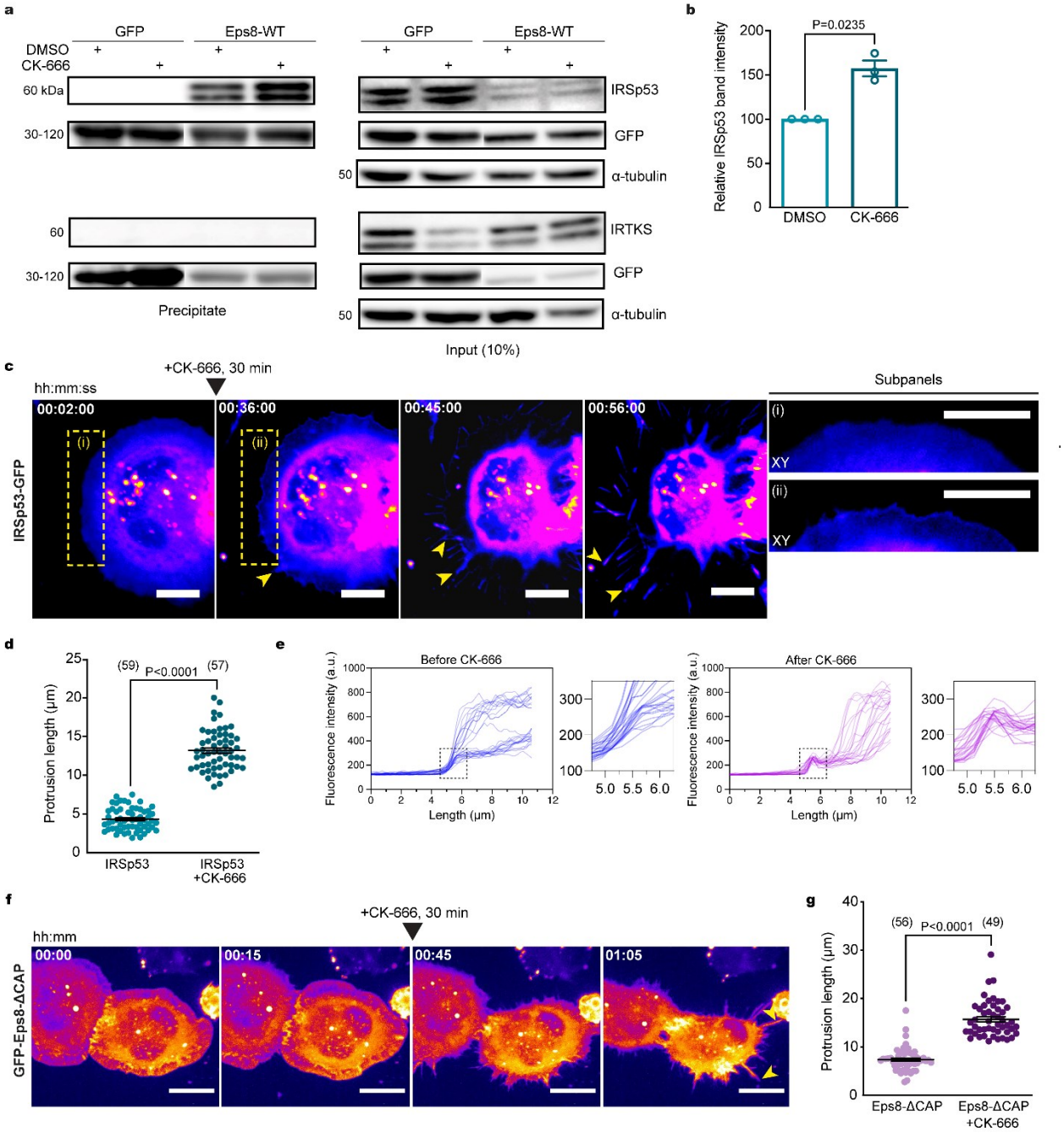

Fig. 4: Eps8 and IRSp53 are recruited to form longer protrusions upon Arp2/3 inhibition. **(a)** Representative Western Blots showing GFP-trap immunoprecipitation bands of the IRSp53 and IRTKS pray proteins in the GFP-Eps8-WT bait precipitate (left) and input lysate (right), with or without 50 μM CK-666 treatment. **(b)** Relative IRSp53 band intensity quantification. Both the CK-666-treated and DMSO-treated bands for IRSp53 were normalized with respect to their Eps8-WT bait bands (detected by an anti-GFP antibody). Relative band intensity was 157.5 ± 8.9% for the CK-666 condition as compared to the DMSO control (was set to 100%). Data are from three individual experiments and are represented as a mean ± SEM. Statistical analysis was performed using a t-test with Welch's correction, P = 0.0235. **(c)** Representative time-lapse images (2, 36, 45 and 56 min from Supplementary Video 7) of protrusion formation in IRSp53-transfected cells

before and after CK-666 addition (at 30 min). Yellow arrowheads show protrusions that are formed after CK-666 addition. Subpanels (i, ii) show the enlarged sections of the cell edge before (i) and after (ii) the addition of CK-666, demonstrating the recruitment of IRSp53 at the membrane (ii). **(d)** Scatter plot comparing the maximum protrusion length before (4.3 ± 0.2 μm) and after CK-666 addition (13.2 ± 0.3 μm) in IRSp53-transfected cells containing the F-actin label tdTomato-F-tractin. Twenty-five cells were analysed, and the number of protrusions analysed in each condition is indicated in parentheses. Data are from 10 individual experiments and are represented as a mean ± SEM. Statistical analysis was performed using an unpaired t-test with Welch's correction, $P < 0.0001$. (**e**) Profile plots of IRSp53 intensity determined across the membrane before (left) and after the addition of CK-666 (right). Magnified views of the cell edge (dashed black boxes) are provided to better highlight the recruitment of IRSp53 at the cell membrane in the CK-666 condition as compared to the control. Two cells were analysed: before CK-666, 28 measurements; after CK-666, 25 measurements. **(f)** Representative time-lapse images (0, 15, 45 and 65 min from Supplementary Video 8) of protrusion formation in Eps8-ΔCAP-transfected cells before and after CK-666 addition (at 30 min). Yellow arrowheads show protrusions that are formed after CK-666 addition. **(g)** Scatter plot comparing the maximum protrusion length before (7.4 ± 0.3 μm) and after CK-666 addition (15.7 ± 0.5 μm) in Eps8-ΔCAP-transfected cells containing the F-actin label tdTomato-F-tractin. Twenty-one cells were analysed, and the number of protrusions analysed in each condition is indicated in parentheses. Data are from 9 individual experiments and are represented as a mean ± SEM. Statistical analysis was performed using unpaired t-test with Welch's correction and P value < 0.0001. Scale bars: (**c**) 10 μm, Insets, 10 μm; (**e**) 20 μm.

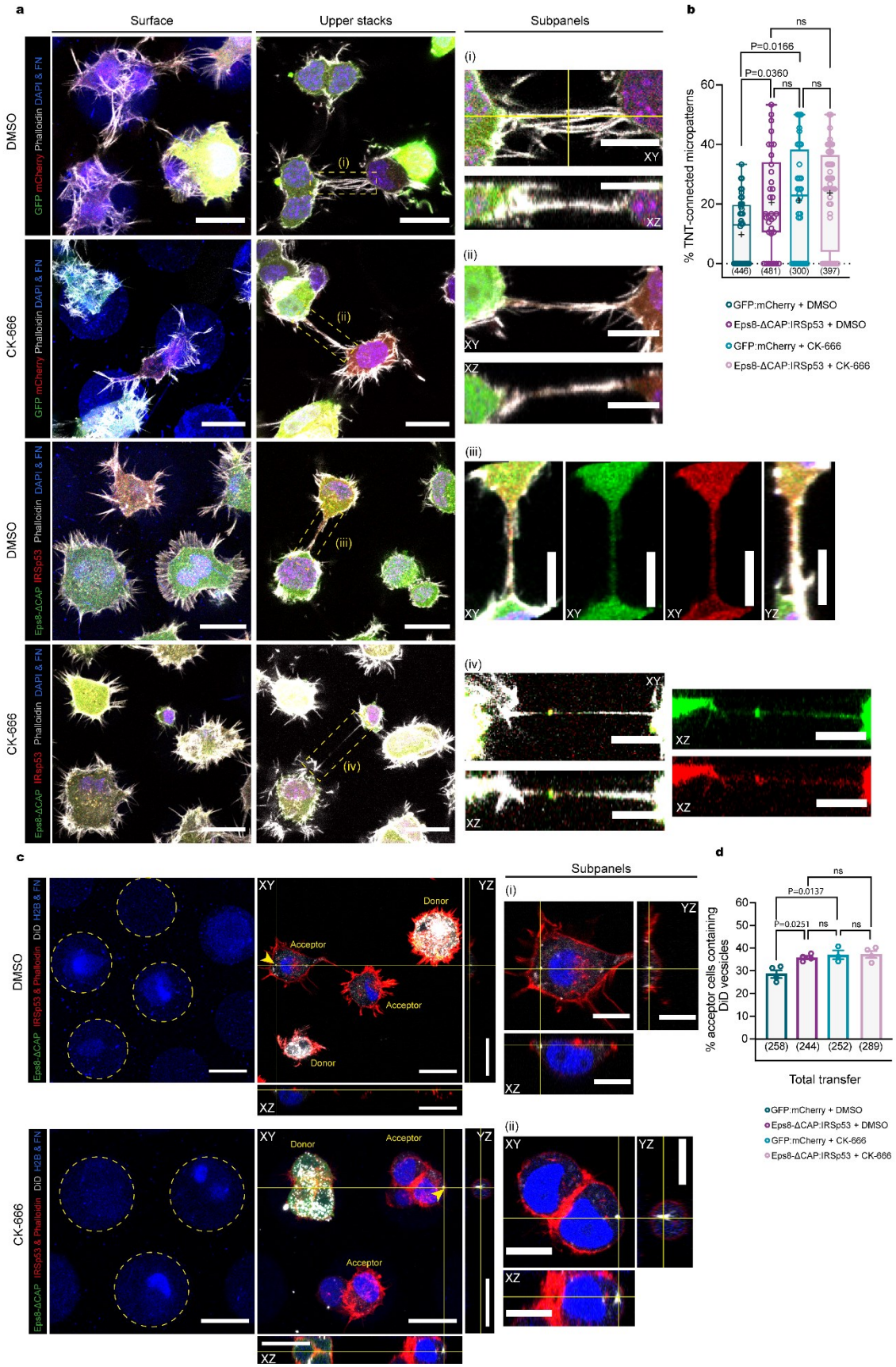
a
Surface
Upper stacks
Subpanels
DMSO
CK-666
GFP mCherry Phalloidin DAPI & FN
Eps8-ΔCAP IRSp53 Phalloidin DAPI & FN
(i)
(ii)
(iii)
(iv)
XY
XZ
YZ
b
% TNT-connected micropatterns
P=0.0166
P=0.0360
ns
(446) (481) (300) (397)
GFP:mCherry + DMSO
Eps8-ΔCAP:IRSp53 + DMSO
GFP:mCherry + CK-666
Eps8-ΔCAP:IRSp53 + CK-666
c
Eps8-ΔCAP IRSp53 & Phalloidin DiD H2B & FN
Donor
Acceptor
d
% acceptor cells containing DiD vecsicles
P=0.0137
P=0.0251
(258) (244) (252) (289)
Total transfer

1331

1332 **Fig. 5: Eps8–IRSp53 co-expression leads to the formation of functional TNT-like protrusions**
1333 **on micropatterns.**
1334 **(a)** Representative surface and upper stack images of control GFP:mCherry and GFP-Eps8-
1335 ΔCAP:IRSp53-mCherry expressing CAD cells plated on *D*15 micropatterns (Alexa 405-labelled
1336 FN) treated with either DMSO or CK-666. Subpanels (i–iv) show magnified projections of the
1337 TNTs indicated in the dashed yellow boxes; XZ and YZ projections were made through the axis
1338 of the TNT. **(b)** Whisker box plot of the percentage of TNT-connected cells on *D*15 micropatterns
1339 for GFP:mCherry + DMSO (10.3 ± 1.6%), Eps8-ΔCAP:IRSp53 + DMSO (20.8 ± 2.8%),
1340 GFP:mCherry + CK-666 (21.4 ± 3.1%), and Eps8-ΔCAP:IRSp53 + CK-666 cells (23.5 ± 2.4%)
1341 (mean ± SEM). Total number of quantified cells on patterns is indicated below the Whisker plots
1342 for each condition. Data were pooled from 3 individual experiments and each data point
1343 corresponds to a quantified image in which on average approximately 10 cells were within the
1344 acquired field of view. Mean values are indicated as a + symbol on the graph for each condition.
1345 Statistical analysis was performed using a Kruskal Wallis test with Dunn's multiple comparison
1346 test. Significant P values for each comparison are stated on the plot, ns = non-significant for P >
1347 0.9999. **(c)** Representative images of GFP-Eps8-ΔCAP:IRSp53-mCherry donor cells co-cultured
1348 with H2B-EBFP acceptors treated with either DMSO or CK-666. Dashed yellow circles annotate
1349 Alexa 405-labelled FN patterns for clarity and yellow arrowheads show the donor-originating
1350 vesicle in the acceptor cell. Subpanels (i, ii) show magnified projections of the acceptor cell
1351 containing DiD-labeled vesicles (yellow arrowheads); XZ and YZ projections were made through
1352 the vesicle. **(d)** Bar graph showing the percentage of H2B-EBFP acceptors containing DiD-stained
1353 vesicles in GFP:mCherry + DMSO (28.8 ± 1.7%), Eps8-ΔCAP:IRSp53 + DMSO (35.7 ± 0.7%),
1354 GFP:mCherry + CK-666 (37.0 ± 1.9%), and Eps8-ΔCAP:IRSp53+CK-666 (37.2 ± 1.5%)
1355 experiments. Total number of quantified acceptor cells is indicated for each condition. Data are
1356 from at least 3 individual experiments and are represented as a mean ± SEM. Statistical analysis
1357 was performed using an ordinary ANOVA with Tukey's multiple comparison test. Significant P
1358 values for each comparison are stated on the bar graph. ns = non-significant for GFP:mCherry +
1359 CK-666 vs. Eps8-ΔCAP:IRSp53 + DMSO, P = 0.9246; for GFP:mCherry + CK-666 vs. Eps8-
1360 ΔCAP:IRSp53 + CK-666, P = 0.9999; and for Eps8-ΔCAP:IRSp53 + DMSO vs. Eps8-
1361 ΔCAP:IRSp53 + CK-666, P = 0.8807. Scale bars, 20 μm; Subpanels, 10 μm.
1362

1363

1364

1365

1366

1367

1368

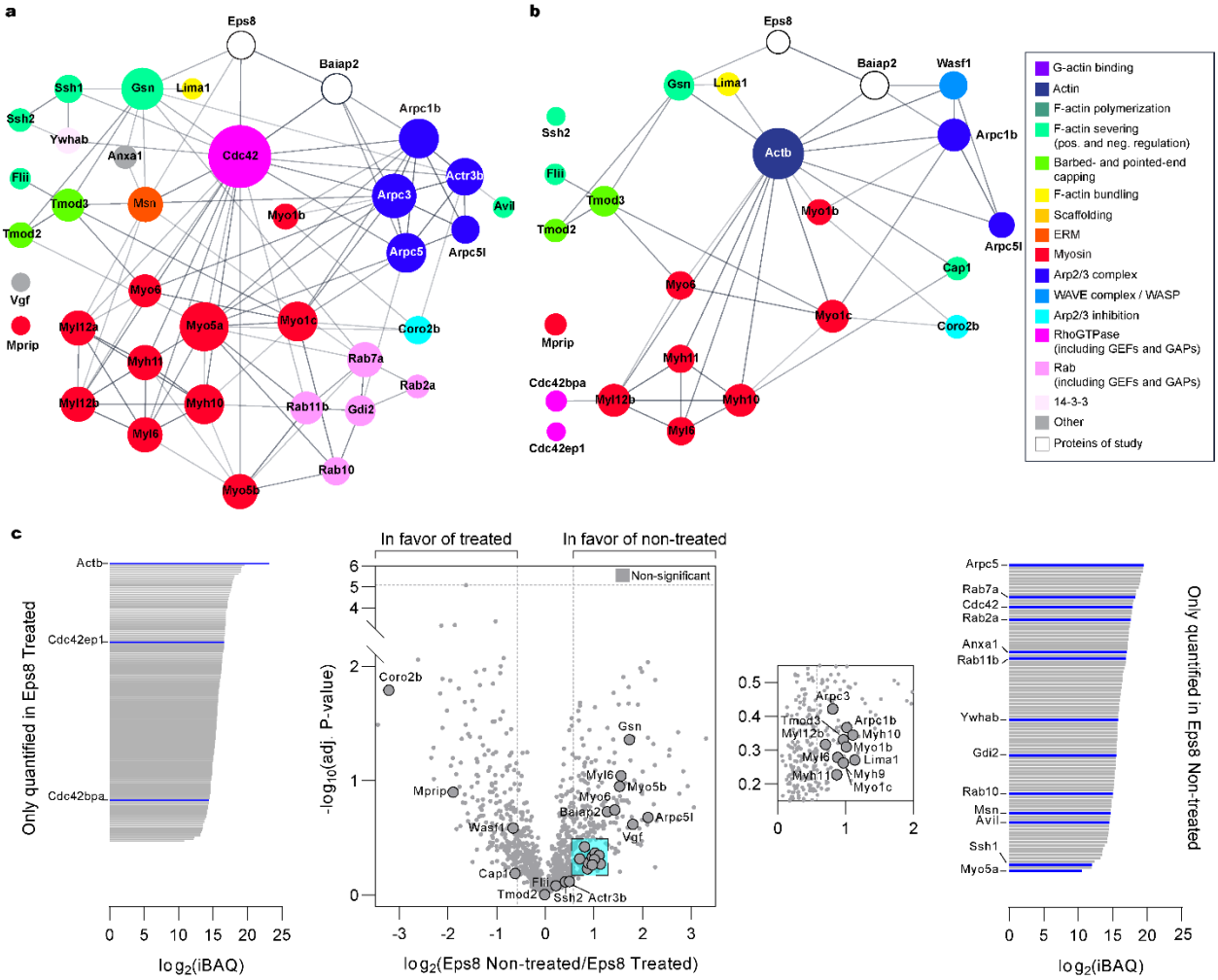

Fig. 6: Eps8's interactome reveals a weakened interaction with Arp2/3 complex components and proteins affecting filament turnover and depolymerization upon CK-666 treatment. **(a)** STRING-generated networks of differentially abundant proteins present in Eps8-WT as compared to the negative control for non-treated (DMSO) (**a**) and CK-666-treated (**b**) CAD cells. The sizes of the nodes (i.e., protein gene names) were scaled based on the degree of connectivity in the networks, and the transparency of the edges relate to the calculated score of the protein-protein interaction in the STRING database. (**c**) Direct comparison of identified protein hits between non-treated and treated Eps8 samples. Left: iBAQ plot of proteins only present in the Eps8 treated sample. Center: Volcano plot of common proteins to both non-treated and treated Eps8 samples. Dashed vertical lines mark the binary logarithm position of a fold change of 1.5, and the dashed horizontal lines marks the adjusted P-value threshold. Cyan-shaded square corresponds to a magnified view of the indicated region on the right of the volcano plot. Right: iBAQ plot of proteins only present in the Eps8 non-treated sample.

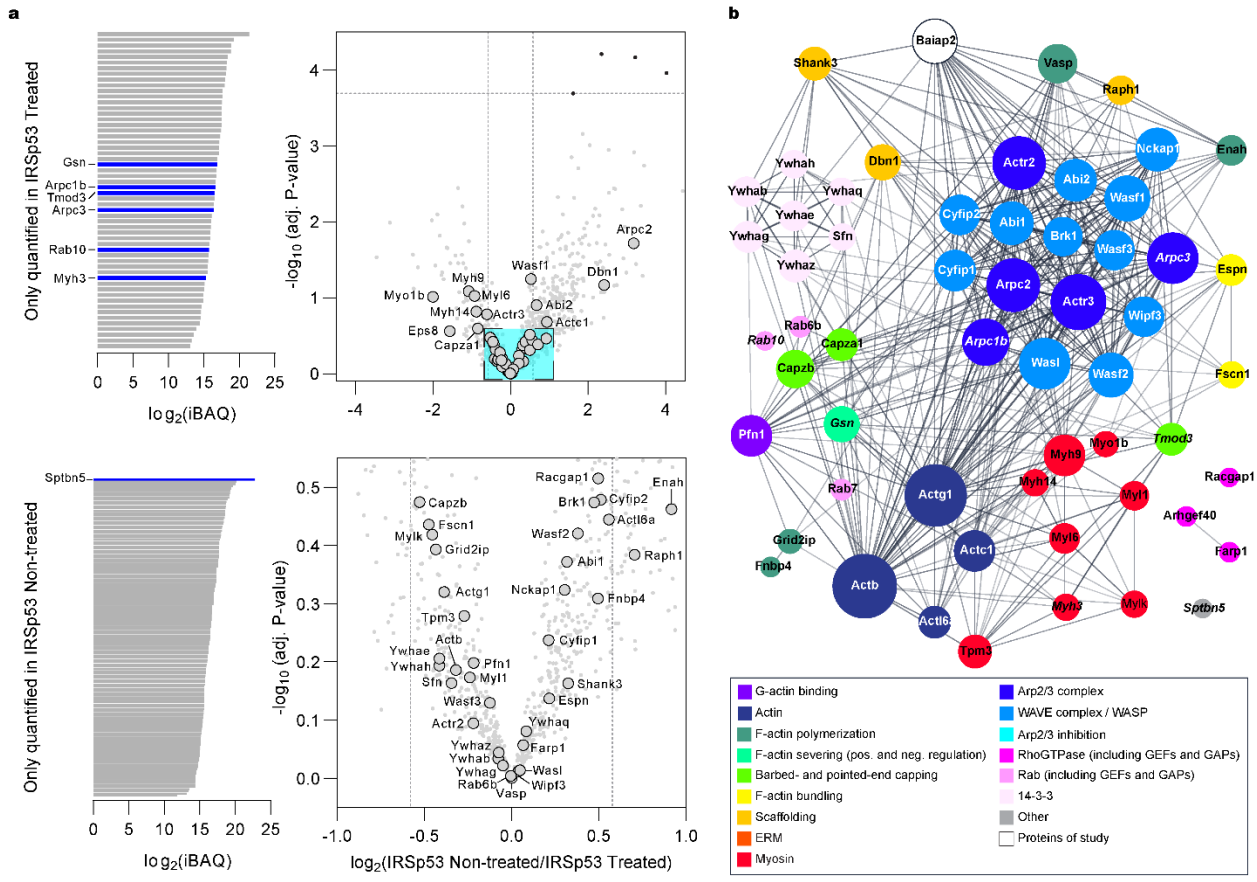

Fig. 7: IRSp53's interactome remains invariant to Arp2/3 inhibition.
(a) Direct comparison between non-treated and treated IRSp53 samples. Left: iBAQ plot of proteins only present in the treated (top) and non-treated (bottom) IRSp53 samples. Right: Volcano plots of common proteins to both non-treated and treated IRSp53 samples. Dashed vertical lines mark the binary logarithm position of a fold change of 1.5, and the dashed horizontal line marks the adjusted P-value threshold. Cyan-shaded square corresponds to a magnified view of the indicated region. **(b)** Combined STRING-generated network of all identified protein hits in the IRSp53 pull down (both non-treated and treated samples). The sizes of the nodes (i.e., protein gene names) were scaled based on the degree of connectivity in the networks, and the transparency of the edges relate to the calculated score of the protein-protein interaction in the STRING database. Italicised hits are those proteins present only in the treated (e.g., Gsn, Arpc1b, Arpc3, Tmod3, Rab10, Myh3) or non-treated (e.g., Sptbn5) IRSp53 sample shown in **a**.